ABSTRACT

Title of Document: *SOME MECHANICS CHALLENGES AND SOLUTIONS IN FLEXIBLE ELECTRONICS*

Matthew Brody Tucker, Master of Science, University of Maryland, 2009

Directed By: Prof. Teng Li, Department of Mechanical Engineering, University of Maryland

Flexible electronics is an emerging field with potential applications such as large area flexible displays, thin film solar panels, and smart prosthesis, to name a few. Promising future aside, there are challenges associated with flexible electronics including high deformability requirements, needs for new manufacturing techniques and high performance permeation barriers. This thesis aims to explore possible solutions to address these challenges. First, a thin stiff film patterned with circular holes is proposed as a deformable platform to be used in flexible electronics in either component and circuit level. Second, we explore possible pathways to improve the quality of transfer printing, a nanofabrication technique that can potentially enable roll-to-roll printing of flexible devices. Third, we investigate the failure mechanism of multilayer permeation barriers for flexible electronics and offer an improved design to achieve better mechanical reliability.

SOME MECHANICS CHALLENGES AND SOLUTIONS IN FLEXIBLE ELECTRONICS

By

Matthew Brody Tucker

Thesis submitted to the Faculty of the Graduate School of the
University of Maryland, College Park, in partial fulfillment
of the requirements for the degree of
Master of Science in
Mechanical Engineering
2009

Advisory Committee:
Professor Teng Li, Chair
Professor Aris Christou
Professor F. Patrick McCluskey
Dr. Daniel R. Hines

© Copyright by
Matthew Brody Tucker
2009

Dedication

I would like to dedicate this thesis to my best friend, my life partner, my drinking buddy (though not this year), my soul mate, my biking, walking and hiking partner, my daily motivation, my ground, my inspiration, my love, and my wife – Meg. The nearly five years of graduate classes and over two years of research has affected both my life and yours.

Thank you for the patience you showed for the time I spent in the books or on the board. Thank you for the dinners you made alone. Thank you for understanding that any frustrations I showed should not have been seen by you; although they may have passed through my filter occasionally.

Finally, thank you for your support. You knew I had it in me to finish this Master's degree, and I was not going to be satisfied until I was done. May this accomplishment open more doors in our life together so that we may serve the greater good, use our powers for good and not evil, and so on, and so forth.

Acknowledgements

First and foremost, I would like to thank Dr. Li for his time and dedication to this research. Dr. Li spent many hours over the past two years teaching me a field, analysis tool, and research methodology that will remain useful throughout my career. His guidance has helped me learn how to conduct thorough research to create small, but possibly important steps in the development of a new technology. He has taught me that minor contributions to a specialized topic eventually lead to global technological advances.

I would also like to acknowledge all my teachers throughout the years who either taught me a lot in class, or taught me how to learn subjects on my own accord. Both techniques are needed for an effective pursuit of knowledge.

Most importantly, I would like to acknowledge my parents who provided me a solid foundation based on life-long learning and hard work. Without their dedication, I would not be where I am today.

Table of Contents

Dedication .... *ii*
Acknowledgements .... *iii*
Table of Contents .... *iv*
List of Tables .... *vi*
List of Figures .... *vi*
Chapter 1: Introduction to Flexible Electronics *1*
1.1 What are Flexible Electronics? 1
1.2 Mechanics Challenges in Flexible Electronics 6
1.2.1 Challenges of Poor Deformability 6
1.2.2 Challenge for New Manufacturing Techniques 9
1.2.3 Challenge for Flexible Device Reliability 11
1.3 Research Topics 13
Chapter 2: Strain Deconcentration in Thin Films Patterned with Circular Holes *15*
2.1 Introduction 15
2.2 Strain Concentration vs. Deconcentration 22
2.3 Thin stiff films with circular holes patterned in a triangular lattice 25
2.3.1 Simulation Model 25
2.3.2 Results 27
2.4 Thin stiff films with circular holes patterned in a square lattice 31
2.5 Discussion 33
2.6 Conclusion 35
Chapter 3: A Quality Map of Transfer Printing *37*
3.1 Background 37
3.2 Methods 44
3.3 Results 49
3.4 Discussion 55
3.5 Concluding Remarks 61
Chapter 4: Failure Mechanisms of Barrier Layers for Flexible Electronics *63*
4.1 Background 63
4.2 Model 69
4.3 Results 73
4.4 Discussion 79
4.5 Conclusion 80
Chapter 5: Concluding Remarks *82*
Publications *87*

Conferences: *87*
Bibliography *88*

List of Tables

Table 1. Maximum failure strains for free-standing Au ,ITO, and Si [8-10] 7
Table 2. Electronic material melting temperatures 10
Table 3. Barrier layer functionality.. 12

List of Figures

Figure 1. Flexible electronic displays 1
Figure 2. Flexible solar panels 2
Figure 3. Readius pocket reader.. 2
Figure 4. Samsung FOLED.. 3
Figure 5. Flexible electronic paper 3
Figure 6. Plastic logic reader 4
Figure 7. Flexible skin-like sensors 5
Figure 8. Cross-section view of a typical transistor.. 6
Figure 9. Crack resulting from a tensile test of a free-standing aluminum film 100nm thick [9]... 7
Figure 10. Cracks resulting from a biaxial tension test of a 100nm thick ITO film [10] 7
Figure 11. Maximum induced strains due to the pure bending of a 1mm thick layer. . 8
Figure 12. Electronic chip fabrication laboratory 9
Figure 13. Roll-to-roll manufacturing of flexible electronics.................................. 10
Figure 14. OLED corrosion spots [13] 12
Figure 15. Three enabling technologies addressed to develop flexible electronics; Increased deformability, enhanced manufacturing techniques, and increased reliability through barrier layer coatings.. 14
Figure 16. Thin metal films stretchability on elastomeric substrates [19]................. 16
Figure 17. Pre-stretched film after release [23] 16
Figure 18. Pre-stretched film resistance plot [23].. 17
Figure 19. An initially planar paper serpentine elongates by deflecting out of plane. The resulting strain in the serpentine is small even though the overall elongation is large. [25] 18
Figure 20. Tri-branch cracking in a gold film bonded to PDMS stretched in tension 20% [26]... 19
Figure 21. Pyrimid features manufactured into an Au film on PDMS to reduce crack propagation [27].. 20
Figure 22. Experimental results of a thin Au film before and after tensile elongation. a) Continuous film prior to elongation. b) Film with patterned holes prior to elongation. c) Continuous film after 30% tensile elongation. d) Film with patterned holes after 30% tensile elongation. (Courtesy of Prof. Sigurd Wagner, Princeton University) 21

Figure 23. (a) Under tension, a blanket thin film with a circular hole stretches *in the plane*, leading to strain concentration near the hole edge up to three times of the applied tension. The strain concentration decays at locations away from the hole edge. (b) In a thin film patterned with an array of circular holes, the film ligaments that demarcate the holes form hidden serpentines (e.g., dotted curves). Such serpentines deflect *out of plane* when the film elongate. As a result, the strain in the film is deconcentrated, even near the hole edges. 22
Figure 24. Serpentines in various directions 24
Figure 25. (a) A thin film patterned with circular holes whose centers coincide with a triangle lattice. The two shaded areas illustrate the simulation models under two representative tensile directions, respectively. (b) Schematic of the simulation model. 26
Figure 26. Deformed shapes of the shaded area in Figure 25b under a relative elongation of 30%, for two deformation modes; (a) In-plane deflections; (b) Out-of-plane deflections. Note the difference in the strain level in the film, as indicated by the color shades. 27
Figure 27. The maximum principal strain $\varepsilon_{\max}$ in the film as a function of relative elongation. For a blanket thin film with a single circular hole, $\varepsilon_{\max}$ is three times of the relative elongation. For a thin film patterned with an array of circular holes, in-plane stretch of the film leads to $\varepsilon_{\max}$ comparable to the relative elongation, while out-of-plane deflection of the film further deconcentrates the strain to only a fraction of the relative elongation. 29
Figure 28. $\varepsilon_{\max}$ in a thin film with circular holes patterned in a triangle lattice as a function of relative elongation, for various *R/L* ratios and two representative tensile directions. 30
Figure 29. (a) A thin film patterned with circular holes whose centers coincide with a square lattice. The two shaded areas illustrate the simulation models under two representative tensile directions, respectively. (b) $\varepsilon_{\max}$ as a function of relative elongation, for various *R/L* ratios and two representative tensile directions. 31
Figure 30. Normalized energy release rate *G/ER* at the microcrack tip as a function of relative elongation. Note the significant difference in the driving force of crack growth for the two deformation modes. G_c denotes the threshold value above which the microcrack grows under monotonic loading. 34
Figure 31. Crack tip stress contour 34
Figure 32. (a) Schematic of a transfer printing process that consists of two steps: (1) A printable layer is sandwiched in between a transfer substrate and a device substrate under pressure and elevated temperature; (2) The structure is cooled and the transfer substrate is lifted off. After such a process, the printable layer can be either successfully transferred, or partially transferred, or unsuccessfully transferred onto the device substrate. (b) (From right to left) Optical images of the silicon transfer substrates (bright region) and the remaining printable layer of poly(methyl methacrylate) (PMMA, dark region) after successful, partially successful, and unsuccessful transfer printing onto a poly(ethyleneterephthalate) (PET) device substrate, respectively. The percentage area of PMMA layer transferred onto the PET substrate are 95%, 67% and 5%, respectively, in these three cases. The size of the

silicon transfer substrates are roughly 1 cm by 1 cm. The thicknesses of the PMMA layer and the PET device substrate are approximately 600 nm and 150 μm, respectively. In the successful case, the surfaces of both the printable layer and the device substrate were O_2 plasma-treated to improve adhesion; in the partial transfer printing case, only the device substrate surface was O_2 plasma-treated; while in the unsuccessful case, no surface treatment was applied... 38
Figure 33. Differential adhesion of two different materials 40
Figure 34. Kinetically controlled transfer printing a) Fast rate picks up film; b) Slow rate prints film; c) Film/substrate energy release rate vs. velocity [41]..................... 41
Figure 35. Schematic of the interface cracks in the transfer printing computational model (not in scale)... 44
Figure 36. Transfer printing FEA model mesh size.. 47
Figure 37. Transfer printing FEA crack mesh size 48
Figure 38. Solid lines: normalized energy release rate $G_b / E_{PL}\varepsilon^2 h$ of an edge crack at the bottom interface as a function of normalized crack length L_b / h, for various device substrate stiffness. No crack exists at the top interface; Dashed lines: $G_t / E_{PL}\varepsilon^2 h$ as a function of L_t / h for an edge crack at the top interface, for various device substrate stiffness. No crack exists at the bottom interface............................ 50
Figure 39. Normalized energy release rates $G_b / E_{PL}\varepsilon^2 h$ of an edge crack at the bottom interface and $G_t / E_{PL}\varepsilon^2 h$ of an edge crack at the top interface as functions of the normalized bottom interfacial crack length L_b / h for various top interfacial crack lengths and device substrate materials... 52
Figure 40. Von Mises stress field near the interfacial cracks for various crack length combinations. Here $E_{DS} = 2.6\,GPa$, $L_t / h = 20$. Color shades: red indicates high stress level and blue indicates low stress level. When $L_b / h < L_t / h$, the high stress concentration near the tip of the top interfacial crack remains approximately unchanged, while the stress level near the tip of the bottom interfacial crack is low. When $L_b / h = L_t / h$, stress concentration occurs at both crack tips. Note the maximum shielding effect of the top interfacial crack to the bottom interfacial crack when $L_b / h = 16$... 54
Figure 41. G_t / G_b as a function of L_b / h for various device substrates. Here $L_t / h = 20$. The dashed line denotes the case of equal interfacial adhesion energy $G_t^c / G_b^c = 1$. 56
Figure 42. A quality map of transfer printing. Each curve defines a boundary line in the space of L_b / h and L_t / h, for a given E_{DS} and G_t^c / G_b^c, below which transfer printing is expected to be successful and otherwise unsuccessful............................ 58
Figure 43. Top: Picture of a set of OLED pixels as-made; Bottom: After only 140 hours of operation, dark spots appear in the OLED pixels. The size of the dark spots continuously grow with time. [51].. 63
Figure 44. OLED luminance versus time using different barrier layers technology [48]... 64
Figure 45. Hybrid barrier layer made from multiple dyads of inorganic/organic layers (Vitex Systems, Inc.).. 65

Figure 46. (a) Vapor diffusion paths through the defects in the Al_2O_3 layer of a dyad. (b) The multilayer geometry provides an effective diffusion path much longer than the polymer layer thickness when the defects in adjacent Al_2O_3 layers are widely spaced [52]. 66
Figure 47. A channel crack creates a line source where the water vapor could bond to the Al_2O_3 while debonding creates an area where water could easily pass through the organic layer........ 67
Figure 48. Crack propagation mode analysis in barrier layers [53]........ 68
Figure 49. Schematic of hybrid barrier layer model. 69
Figure 50. Delamination FEA model setup without a protective layer added to the barrier layer 70
Figure 51. Delamination FEA model setup with protective layer added to the barrier layer........ 71
Figure 52. Two delamination cracks in a barrier layer with a protective layer 72
Figure 53. Modeling of a tunneling crack through the inorganic layer of a hybrid barrier layer 73
Figure 54. Delamination results for non-protected barrier layers........ 74
Figure 55. One delamination crack with a protective layer 75
Figure 56. One delamination crack in a barrier layer with a protective layer 75
Figure 57. Energy release rate of one delamination crack with various protective layer stiffness 77
Figure 58. Two delamination cracks with a protective layer........ 78
Figure 59. Energy release rate of a tunneling crack through an inorganic layer both with and without a protective layer........ 79
Figure 60. Three enabling technologies addressed to develop flexible electronics; Increased deformability, enhanced manufacturing techniques, and increased reliability through barrier layer coatings........ 86

Chapter 1: Introduction to Flexible Electronics

1.1 What are Flexible Electronics?

The study of flexible electronics is the culmination of the materials science, electronics, mechanics, and manufacturing fields toward the creation of electronic circuits fabricated on flexible substrates. Flexible electronics have the potential to outperform their traditional rigid counterparts in terms of flexibility, weight, and cost. Potential applications of flexible electronics include paper-like video displays, skin-like smart prosthesis, and printable thin-film solar cells, to name a few [1-5]. Flexible electronics displays or screens as shown in Figure 1 could roll into small volumes saving both space and weight. This would reduce the need for large, bulky traditional screens. Rollable screens could create space savings for television screens, computer monitors, or solar panels [2,6].

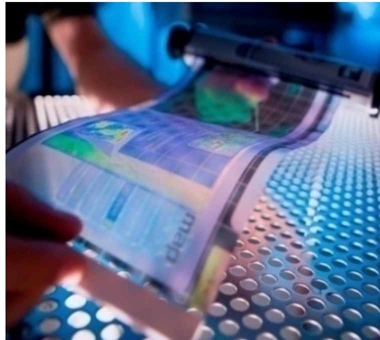

(http://www.psfk.com/2008/12/hp-and-asu-release-first-prototype-of-flexible-electronic-display.html)

Figure 1. Flexible electronic displays

Flexible electronics are emerging into the mainstream market. For example, Figure 2 shows a flexible solar panel currently available to the consumer. A conventional solar panel typically consists of a large rigid rectangular plate; by contrast a flexible solar panel can be rolled into a tube that is a fraction of its normal size. Additionally, the

flexibility of the solar panel could allow it to conform to various shapes (like roofs of cars and houses).

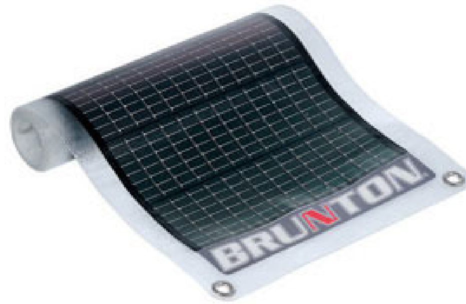

(http://www.brunton.com/product.php?id=256)

Figure 2. Flexible solar panels

Polymer Vision, Inc., a spin-off company of Philips, Inc., has created the Readius, a pocket reader capable of holding 8 Gigabytes of reading material shown on a 5” folding display as shown in Figure 3. The flexibility of the screen allows for a wider display area stored inside a smaller package.

(www.readius.com)

Figure 3. Readius pocket reader

Samsung has unveiled prototype flexible organic light emitting diode (FOLED) displays, as seen in Figure 4, at conventions. Although they are not quite ready for

commercial sales, as explained later, there is much interest in by the public for thin flexible displays.

(http://www.oled-display.net/flexible-oled)

Figure 4. Samsung FOLED

Flexible electronics could also be used to simulate a sheet of paper, as shown in Figure 5. With electronic media readily available, one could receive daily news, books, or other reading material through wireless communications. Unlike emissive displays that can create eye strain, electronic paper would allow comfortable reading using reflected light and increased resolution.

(http://e-paper23.blogspot.com/)

Figure 5. Flexible electronic paper

Plastic Logic plans to start selling its version of an eReader in a pilot program in the second half of 2009 while increasing the sales in 2010 according to their website

(http://www.plasticlogic.com/ereader/index.php). Figure 6 shows the rigid eReader planned for sale on the left and the flexible inner working layer on the right. Their literature claims to use "high-resolution transistor arrays on flexible plastic substrates," however, the working layers are encased in a rigid frame with limited flexibility.

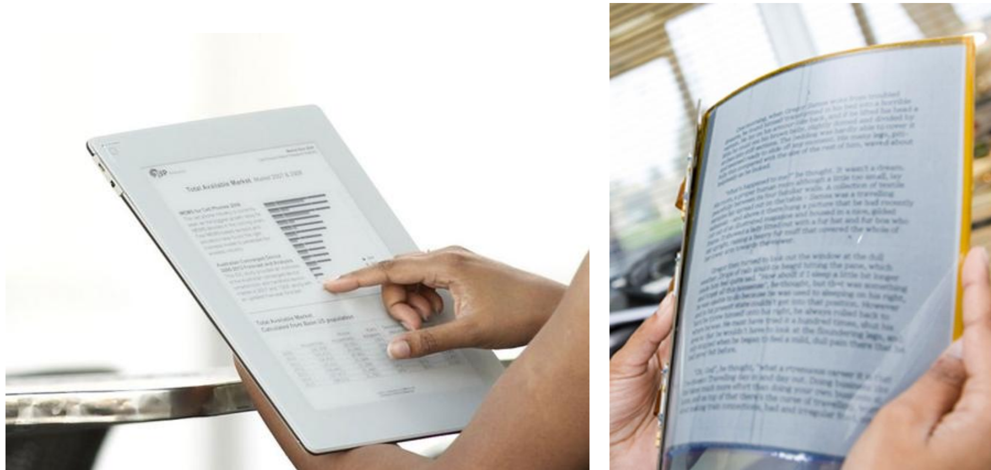

(http://www.gizmag.com/plastic-logic-flexible-electronic-reading-device/9963/gallery/)

Figure 6. Plastic logic reader

A different use for flexible electronics involves placing an electronic skin around prostheses as shown in Figure 7. Flexible electronic sensors could permit the "skin" of the prosthesis to bend and flex like normal skin while allowing for electronic feedback with regard to pressure, temperature, and moisture. Likewise, flexible electronic clothing could provide an array of functions including generating power from solar cell patches and monitoring human health through heart, lung, temperature, and perspiration sensors [7].

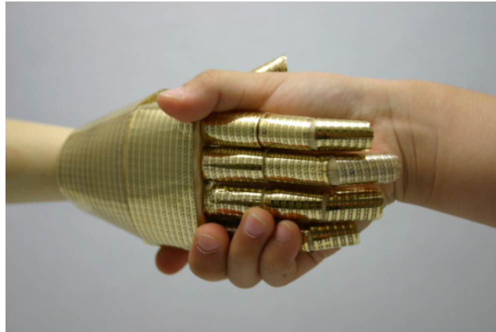

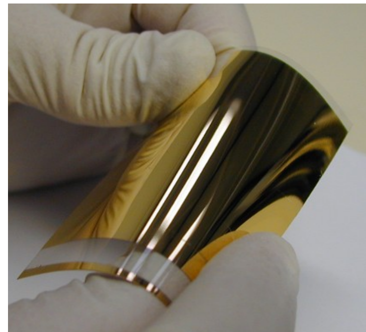

(http://radio.weblogs.com/0105910/2004/09/22.html) (http://www.plasmaquest.co.uk/news.shtml)

Figure 7. Flexible skin-like sensors

The above examples illustrate the plethora of uses for flexible electronics. Flexible electronics differ from conventional electronics in their ability to allow for large deformations. They tend to use more compliant materials as the building blocks of the circuits like polymers and elastomers which sustain large deformations without cracks or failures. Flexible electronics often consists of a large amount of microelectronic components integrated over large areas such as video or reading displays. Finally, flexible electronics often have thin profiles, to achieve better flexibility and to reduce volume (also weight).

Existing work in flexible electronics mainly focuses on the development and prototype phase. The products that do make it to the mainstream market tend to have a limited radius of curvature as shown with the Radius and the eReader, and a high price tag. The next section describes some of the challenges faced by flexible electronics in their advancement to the mainstream market.

1.2 Mechanics Challenges in Flexible Electronics

1.2.1 Challenges of Poor Deformability

Traditionally, electronic circuits have been created using rigid, non-compliant materials such as silicon, as shown in Figure 8. Silicon has an elastic modulus of about 130 GPa, with a maximum failure strains about 4% [8].

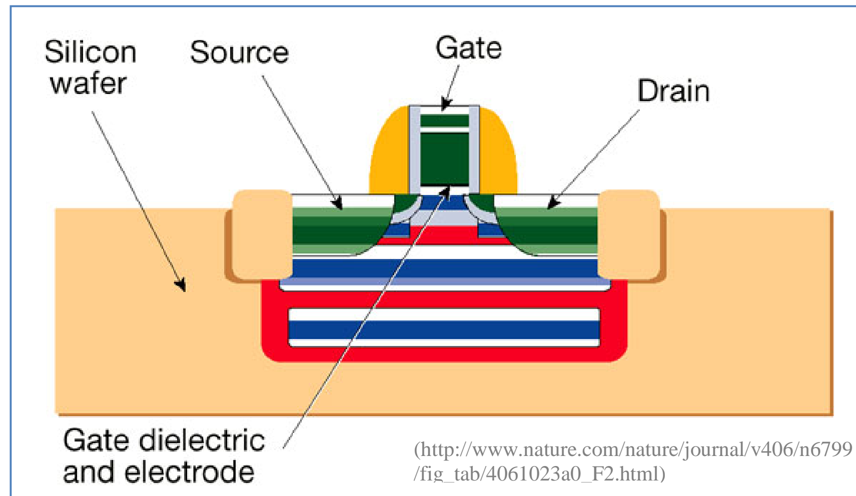

Figure 8. Cross-section view of a typical transistor

Silicon wafers are not the only material used to make in electronic devices. Inorganic materials such as gold (Au) and indium-tin-oxide (ITO) are used extensively in electronic circuits as conductors. For example, ITO conductors are transparent allowing interconnects to be used in front of or behind the emissive layers in displays without interference. Both types of conductors are brittle in the nano-scale, therefore susceptible to cracking, as shown in Figure 9 and Figure 10.

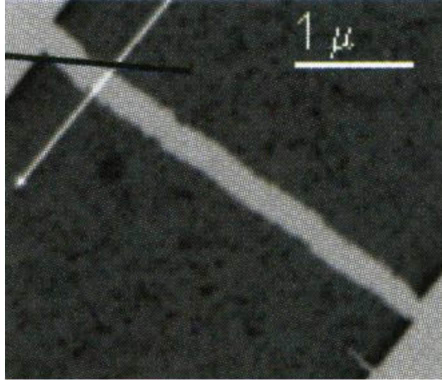

Figure 9. Crack resulting from a tensile test of a free-standing aluminum film 100nm thick [9]

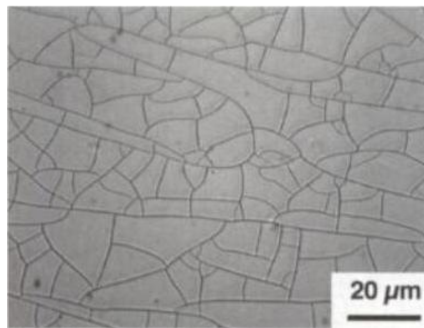

Figure 10. Cracks resulting from a biaxial tension test of a 100nm thick ITO film [10]

The maximum tensile failure strains of the above materials are listed in Table 1 [8-10]. Notice how the the commonly used conductor materials can only sustain tensile strains of approximately 1% before failure. This leaves practically no ability to stretch, bend, or twist without complete failure.

Table 1. Maximum failure strains for free-standing Au ,ITO, and Si [8-10]

Material	Maximum failure strain
Au	~1%
ITO	~1%
Si	~4%

Flexible electronics should be able to flex, stretch, and bend to large amplitudes. As an example, Figure 11 shows the maximum strain due to the bending of a 1mm-thick layer. The maximum tensile strain in the layer is up to 5% when it is rolled into a circle with radius 10mm. For a bending radius of 1mm (imagine folding a thin flexible display), maximum tensile strain in the layer could reach up to 50%, much higher than the failure strain of traditional electronic materials.

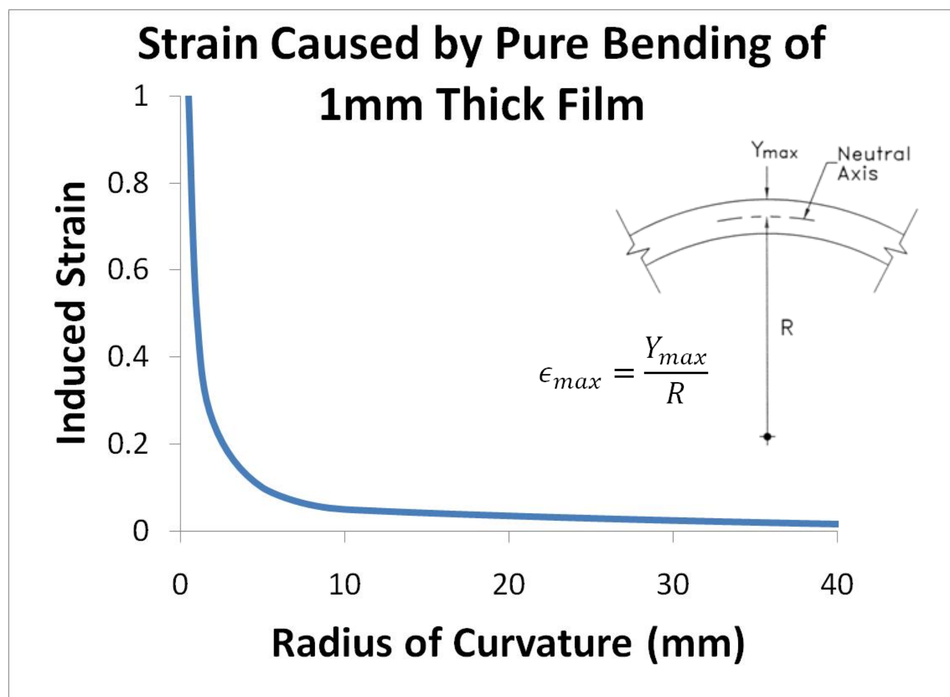

Figure 11. Maximum induced strains due to the pure bending of a 1mm thick layer.

In summary, the mechanics failure of traditional electronic materials under large deformation poses a significant mechanics challenge to the future success of flexible electronics.

1.2.2 Challenge for New Manufacturing Techniques

Traditional microelectronics are fabricated in expensive fabrication facilities (e.g., Figure 12). The process utilized to fabricate electronic chips employs a batch process where one batch at a time is taken through a multi-step process to add each functional layer into the microelectronics components, leading to a time consuming process with high costs.

(http://hsma.hynix.com/hsma/about/corporate_info.jsp)

Figure 12. Electronic chip fabrication laboratory

There are two problems with microelectronics fabrication facilities that hinder their ability to fabricate flexible electronic devices. First, the facilities are designed for certain silicon wafer sizes – typically smaller than that needed for flexible electronic devices. Such facilities are often not scalable to large areas. Second, the fabrication process typically uses high temperatures during thin film deposition. These high temperatures are not suitable for most of the organic materials that are used in flexible electronics.

Most flexible circuits employ compliant organic material such as polyethylene terephthalate (PET) and polymethylmethacrylate (PMMA). The melting temperatures of these organic materials are often lower when compared to silicon and gold (see

Table 2). Conventional manufacturing processes can expect temperatures up to 600 °C [11]. Therefore, conventional deposition methods cannot be used to fabricate thin films of organic materials to be used in flexible electronics.

Table 2. Electronic material melting temperatures

Material	Melting Temperature (°C)
Silicon	1410
Gold	1065
PET	260
PMMA	254

Alternatively, a roll-to-roll printing fabrication process is envisioned as a possible manufacture technique for flexible electronics, as shown in Figure 13. Rolls of flexible materials are placed in an assembly line similar to a newspaper printing press. The functional layers of the electronic devices can be rolled and pressed together to form a functional flexible electronic device. This high speed, efficient technique, if mastered properly, could lead to dramatic cost reductions. Such cost reductions could potentially make flexible electronics more affordable than conventional rigid electronics. Although roll-to-roll printing has not been demonstrated on a full scale, the promise for low cost flexible electronics drives the research into this emerging field.

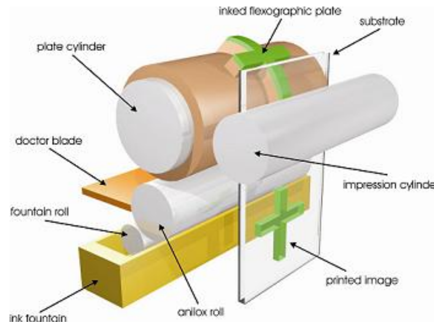

(http://foulger.clemson.edu/article.php?story=20070111121844925)

Figure 13. Roll-to-roll manufacturing of flexible electronics

In summary, the traditional manufacturing techniques are not suitable for flexible electronics. New manufacturing methods have been envisioned that utilize the large area, flexible materials, and low working temperatures associated with flexible electronics. **There is a need to develop low cost, large area, low temperature fabrication methods to address the mechanics challenges of flexible electronics production.**

1.2.3 Challenge for Flexible Device Reliability

To make flexible electronics truly advantageous to conventional rigid electronics, they must show similar performance capability at reduced costs. For flexible displays, organic light emitting diodes (OLEDs) can be used instead of the conventional LCD or plasma screens. The OLEDs have shown increased performance capabilities by measuring display contrast ratio, brightness, and efficiency [2,12].

However, experiments have shown that OLEDs will corrode when not protected adequately from water vapor and oxygen [13-15]. Figure 14 shows the corrosion spots that occur in an OLED coated with a thin barrier layer of ITO on both sides after hours of exposure to the atmosphere. As the spots grew, the luminescence of the OLED decreased until it was deemed unusable.

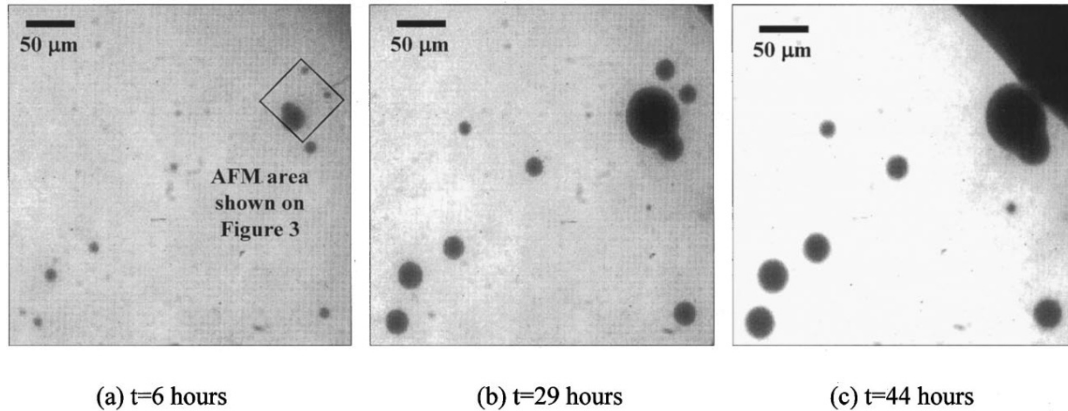

Figure 14. OLED corrosion spots [13]

Traditionally, the entire circuit could be encapsulated in a thick, rigid glass or ceramic coating, however, the rigid coating prevents flexibility. To make FOLEDs, it is therefore favorable to create a barrier layer that is impermeable to water vapor yet flexible. Table 3 below shows the general functionality of various materials. It shows that both bulk organic material like PET and PMMA along with thin (10 nm) inorganics such as aluminum-oxide (AlO_x) and ITO are not impermeable to water vapor transfer but are flexible. They could be used to create FOLEDs capable of functioning on the order of hours before corroding. On the other hand, bulk inorganic materials are impervious to water vapor transfer yet not flexible. They could be used to make traditional OLEDs that can function for years yet unable to flex without failure.

Table 3. Barrier layer functionality

Material	Water impervious	Flexible
Bulk Organic	No	Yes
Bulk Inorganic	Yes	No
Thin Inorganic	No	Yes
Ideal	Yes	Yes

More details associated with barrier layers are discussed in chapter 4. The above description however shows the difficulty associated with barrier layer technology and the need for barrier layers in FOLEDs. **There is a need to overcome the reliability challenges associated with the mechanics of flexible thin film barrier layers.**

1.3 Research Topics

This thesis aims to advance the field of flexible electronics by exploring possible solutions to the above three mechanics challenges. First, challenges and solutions to enhance the deformability of thin stiff films are presented in Chapter 2. These solutions allow conducting materials like Au and ITO to be used without fracture at large deformation. Next, Chapter 3 describes challenges and proposed solutions to a nanofabrication process called transfer printing. Developments in this nanofabrication process can potentially enable roll-to-roll printing which promises to provide dramatic reductions in production costs. Finally, Chapter 4 shows challenges and solutions with regard to a high performance multilayer permeation barrier. Advancements in permeation barrier technology will allow flexible electronics to function reliably over long periods of time while remaining flexible in nature.

Figure 15 depicts the research framework of this thesis, as discussed above.

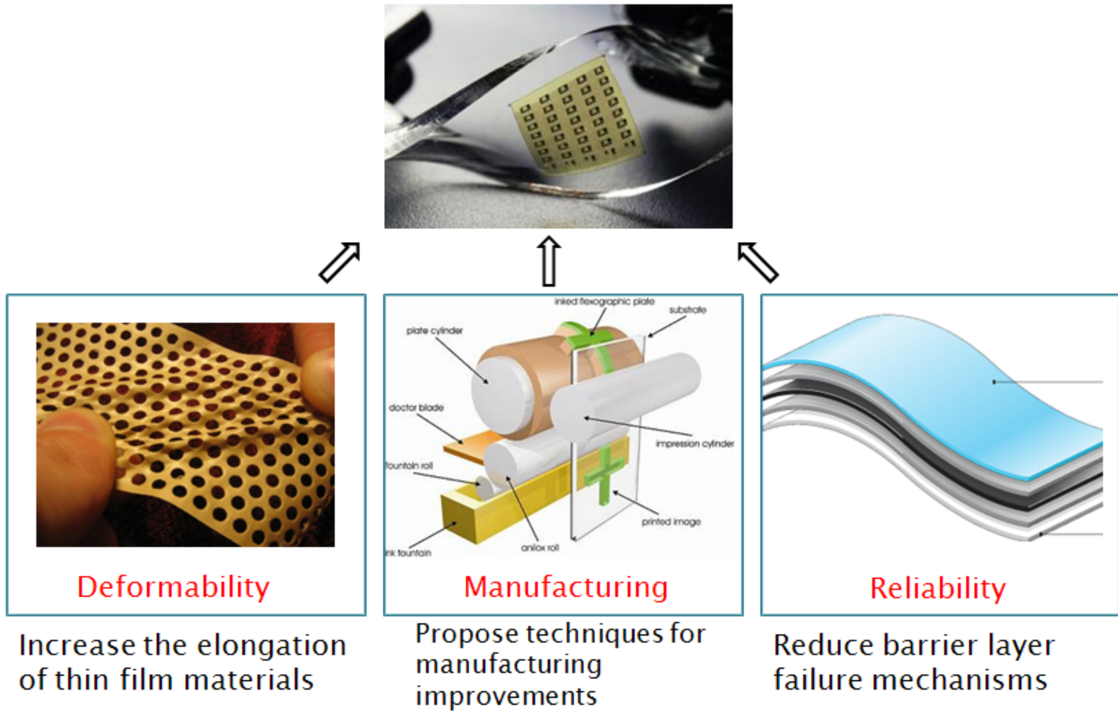

Figure 15. Three enabling technologies addressed to develop flexible electronics; Increased deformability, enhanced manufacturing techniques, and increased reliability through barrier layer coatings.

Chapter 2: Strain Deconcentration in Thin Films Patterned with Circular Holes

2.1 Introduction

Flexible electronics requires the thin film of functional electronic materials (Si, metal, etc) to sustain large elongations during service. Typical thin films of electronic materials fracture at low strains, while flexible electronics need to withstand high strains when they are deformed. Recent research efforts have led to several concepts to improve the deformability of thin stiff films. In an island concept enabling stretchable electronic surfaces, thin device islands of a stiff material (e.g., SiN) are fabricated on a compliant polymer substrate [16-18]. When the entire structure is stretched, the deformation is mainly accommodated by the polymer substrate, and the induced strain in the majority part of a stiff island is small. The resulting strain near the island edges, however, can be significant and may cause the island cracking if the island size exceeds a critical value (e.g., a few hundred microns).

Li et al. showed that bonding a thin ductile film to an elastomeric substrate can increase the overall elongation of the film without fracture [19]. As the film begins to elongate, a single incipient necking region begins to form, although it is arrested by the resistance in the well-bonded elastomer. This gives the opportunity for another necking region to occur. Figure 16 below shows the results from the research where stiffer substrates allow for longer elongations. The stretchability of this film, however, relies on its ductility. Once the film is stretched beyond its yield point, permanent deformation occurs. For flexible electronics, a repeatable elongation method is needed for the thin stiff films.

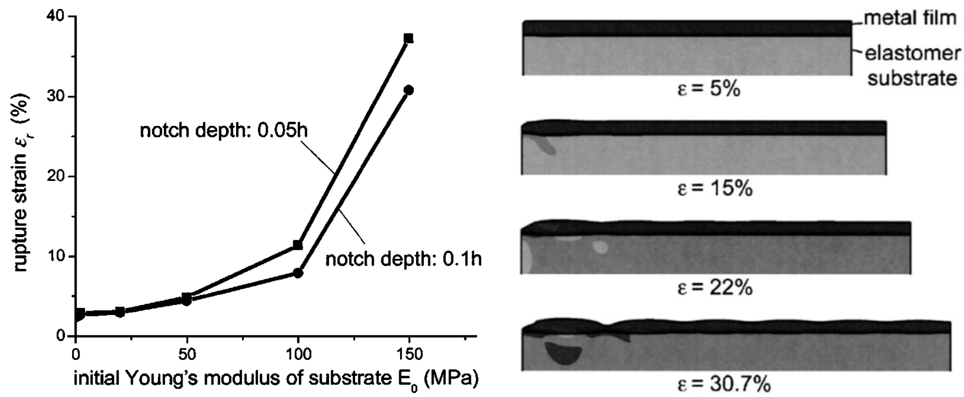

Figure 16. Thin metal films stretchability on elastomeric substrates [19]

In a pre-stretch concept, a thin stiff film is deposited on a rubber-like substrate that is pre-stretched. Upon release of the pre-stretch, a wavy surface pattern forms due to the film wrinkling under the substrate contraction as shown in Figure 17 [20-23]. Such wavy structures can then be stretched up to the pre-stretch strain by flattening the film wrinkles. By controlling the wrinkling shape of the film via controlled interfacial adhesion, uniaxial deformability up to 100 percent can be achieved [24]. A plot of such stretch magnitudes is shown in Figure 18.

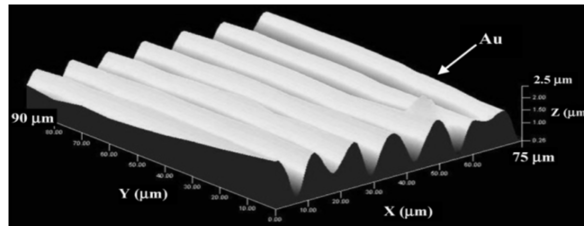

Figure 17. Pre-stretched film after release [23]

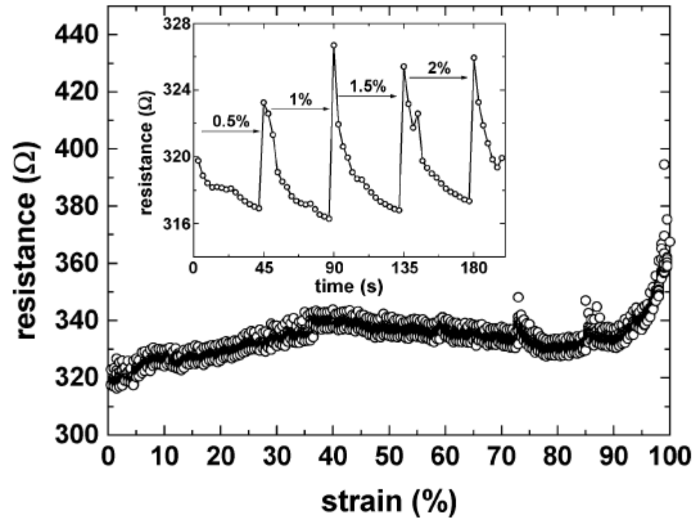

Figure 18. Pre-stretched film resistance plot [23]

The pre-stretch concept, although extremely capable of excessive elongations prior to failure, suffers from a couple of disadvantages. The concept shown in Figure 17 is only wavy in one direction thereby allowing for increased elongations in one direction. Secondly, in its unstretched shape, the film buckles out-of-plane. In a multi-layer electronic functional device, printing or stacking layers on top of a surface that is not smooth poses many challenges. Ideally, all layers in an electronic device should remain planar in their native state for stackability during fabrication.

Recently, Li et al. proposed a general principle to achieve large deformability of thin films of stiff materials by suitably in-plane patterning [25]. As an illustration of this general principle, Figure 19 shows a piece of paper cut into a serpentine, and pulled at the two ends.

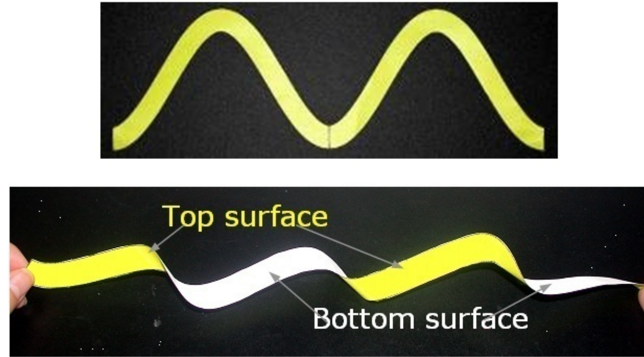

Figure 19. An initially planar paper serpentine elongates by deflecting out of plane. The resulting strain in the serpentine is small even though the overall elongation is large. [25]

While initially planar, the serpentine elongates by deflecting out of plane, so that a large elongation induces only small strains. Simulations show that the maximum strain in the serpentine is ~1% at an elongation of 25%. By contrast, a straight paper stripe breaks at an elongation of only several percent. This above principle solves the problem of increased elongation of thin stiff films, repeatable deformations, and starting off in the planar configuration. The one drawback to this approach is the lack of surface area of the gold film. If this film were to be used as a conductor of electricity, it seems there is more area of substrate than conductor. Likewise, the serpentines would have to be patterned apart from one another to allow for the compliant out-of-plane deformation that reduces local strain in the film.

The patterning principle for increased elongation is also demonstrated by recent experiments of thin gold films (25 nm thick) on elastomeric substrates (1 mm thick) [26]. The surface of the as-fabricated gold film is covered with tri-branched microcracks randomly distributed throughout the film. The gold ligaments that demarcate the cracks, however, form a network that percolates the whole film as shown in Figure 20.

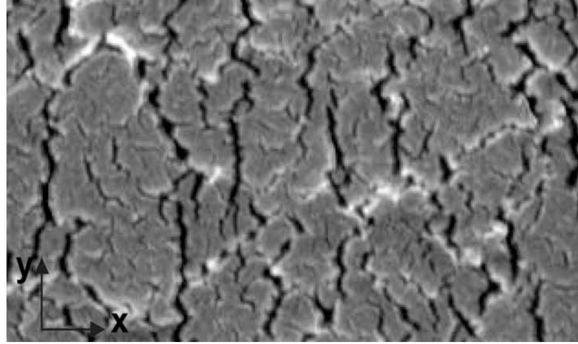

Figure 20. Tri-branch cracking in a gold film bonded to PDMS stretched in tension 20% [26]

Such thin gold films on elastomeric substrates can sustain repeated elongation of 32% for more than 100 cycles without appreciable fracture or fatigue. Further simulations show that the gold ligaments deflect out-of-plane to accommodate the large elongation. As a result, the majority part of the gold film undergoes elastic deformation even though the overall elongation is large. Instead of randomly patterned tri-branched cracks forming during the fabrication process, it would be beneficial if a controllable pattern could be engineered to create increased elongations of thin stiff films.

Mandlik et al. recently fabricated thin gold films with pyramidal features in a geometric pattern on elastomeric substrates as shown in Figure 21 [27]. Such patterned thin gold films can sustain elongations of up to 25% in certain directions while remaining electrically conductive. The enhanced deformability of the gold films is attributed to the pyramids that impede crack propagation in the gold films. The fabrication of such pyramidal features in thin gold films involves multiple lithographical steps, thus is not suitable for high output manufacture.

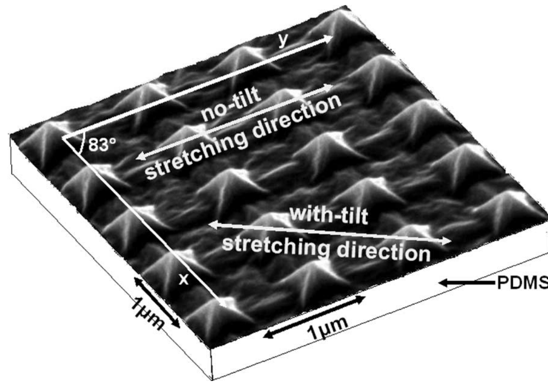

Figure 21. Pyrimid features manufactured into an Au film on PDMS to reduce crack propagation [27]

The above examples demonstrate that the general principle of achieving large deformability of thin stiff films by suitably patterning is essentially geometric, thus independent of materials and length scales. Therefore, it is further proposed that such a deformable thin stiff film can serve as a platform, on which the whole integrated circuit can be fabricated. The resulting architecture can sustain large, repeated deformation without device materials fracture.

In fact, a large variety of patterns allows substantial elongation of thin stiff films by the abovementioned general principle. This chapter investigates the deformability of thin stiff films patterned with an array of circular holes. Such patterns are planar, thus can be easily fabricated with two-dimensional microfabrication techniques. Recent experiments (see Figure 22) demonstrated that, a thin gold film (75 nm thick) patterned with circular holes (about 5 um in diameter) on an elastomeric substrate (250 um thick) can sustain elongations of 30% [28]. Under such a large elongation, microcracks appear near the edge of some holes but the majority part of the film remains intact. In contrast, a continuous thin gold film of same thickness on a same substrate suffers from cracking all over the film when subject to such a large elongation. These preliminary experimental results demonstrate the large

deformability of thin stiff films patterned with circular holes. So far, however, quantitative understanding of the parameters that govern the deformability of the patterned thin films (e.g., hole geometry and distribution, tensile directions, and film/substrate relative stiffness etc.) remains elusive.

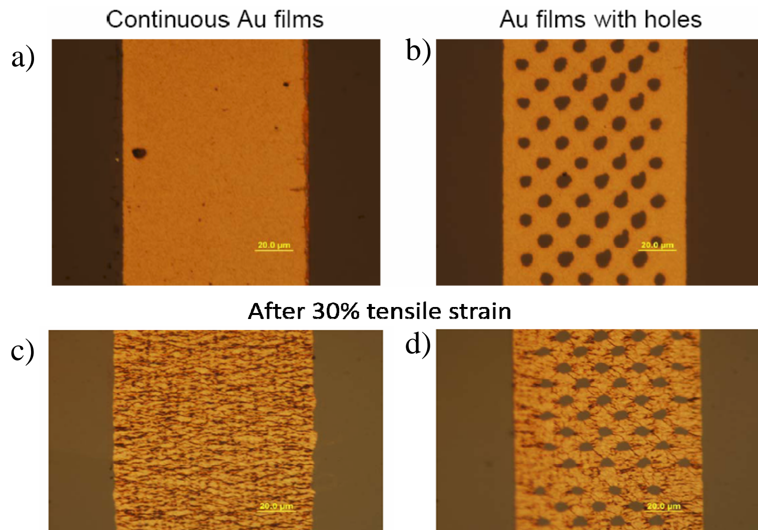

Figure 22. Experimental results of a thin Au film before and after tensile elongation. a) Continuous film prior to elongation. b) Film with patterned holes prior to elongation. c) Continuous film after 30% tensile elongation. d) Film with patterned holes after 30% tensile elongation. (Courtesy of Prof. Sigurd Wagner, Princeton University)

To address the above issues and plan further systematic experiments, the rest of the chapter is organized as follows. Section 2.2 discusses why patterned circular holes in a thin stiff film lead to strain deconcentration, rather than cause strain concentration near the hole edges. Using finite element analysis (FEA) simulations, Section 2.3 studies the effects of hole size, hole spacing, and loading directions on the resulting strain in a thin stiff film with circular holes patterned in a triangle lattice and subject to uniaxial elongation. These results are then compared with those for a thin stiff film

with circular holes patterned in a square lattice in Section 2.4. Further discussions on the driving force for crack growth in the patterned thin films are given in Section 2.5.

2.2 Strain Concentration vs. Deconcentration

It is well known that a circular hole in a thin blanket film results in strain concentration near the hole edge when the film is under tension. The overall elongation of the film is accommodated by pure *in-plane stretch*. The strain level near the circular hole can be as high as three times of the applied tensile strain (see Figure 23a).

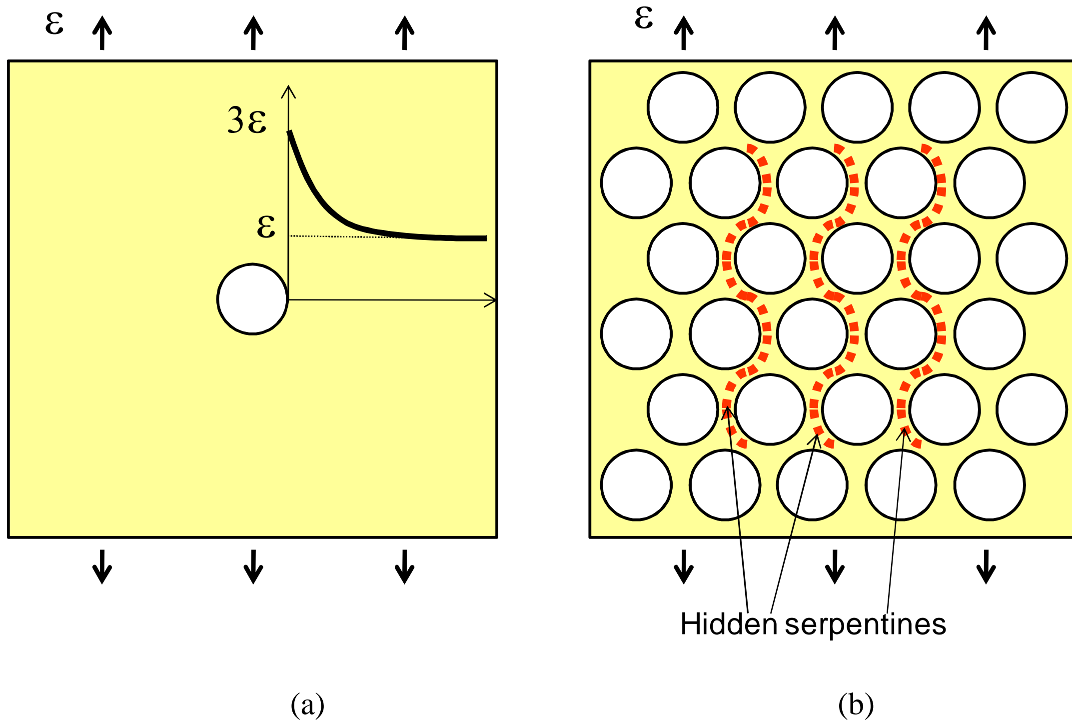

Figure 23. (a) Under tension, a blanket thin film with a circular hole stretches *in the plane*, leading to strain concentration near the hole edge up to three times of the applied tension. The strain concentration decays at locations away from the hole edge. (b) In a thin film patterned with an array of circular holes, the film ligaments that demarcate the holes form hidden serpentines (e.g.,

dotted curves). Such serpentines deflect *out of plane* when the film elongate. As a result, the strain in the film is deconcentrated, even near the hole edges.

The strain concentration near the hole becomes more significant if the hole assumes an elliptic shape. For a thin film with a sharp crack, the limiting case of an ellipse, the strain at the crack tip tends to infinity when such a film is under a finite tension. In contrast, for a thin film patterned with an array of circular holes, the film ligaments that demarcate the circular holes form a network of hidden serpentines (see Figure 23b). When such a film is subject to tension, these hidden serpentines can *deflect out-of-plane* to accommodate the overall elongation (e.g., to be shown in Figure 26a). The resulting strain due to deflection scales with the ratio between thin film thickness and radius of curvature of the deformed film. Under a modest elongation, the radius of curvature of the deformed film is comparable with the feature size of the pattern (e.g., spacing between holes), which is often much larger than the thin film thickness. Consequently, the resulting strain in the film can be significantly deconcentrated, compared to the highly concentrated strain when the film stretches in the plane. For example, as will be shown later, the maximum strain in the film patterned with circular holes can be as low as only half of the applied strain due to tension.

It has been shown that the strain deconcentration in a serpentine under tension (e.g., Figure 19) becomes more substantial if the ratio between the amplitude and the pitch of the serpentine increases (i.e., a more tortuous serpentine) [29]. Similarly, for the film with patterned circular holes under tension, the strain deconcentration becomes more substantial if the circular holes are more densely packed (i.e., more tortuous hidden serpentines). The pattern distribution and the tensile direction also influence

the strain deconcentration in the film. There are hidden serpentines in many directions given a circular hole pattern, as shown in Figure 24, that allow the strain deconcentration to take place given many tensile strain directions.

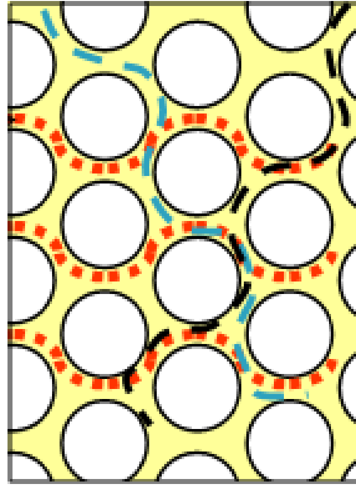

Figure 24. Serpentines in various directions

In practice, patterning a thin stiff film with in-plane features needs to be carried out on the surface of a substrate. The mechanical interaction between the patterned thin stiff film and the underlying substrate strongly influences the deformation behavior of the thin film. If the substrate is too stiff, the film deformation is mainly confined in the plane of substrate surface. As a result, the overall elongation is accommodated by the in-plane stretch, leading to large strains in the film. If the substrate is sufficiently compliant, its surface can be pulled up or pressed down, following the out-of-plane deformation of the thin stiff film. For example, recent simulations show that, under tension, a patterned thin gold film on an elastomeric substrate deforms almost like a freestanding thin gold film with the same pattern. [29]

The next two sections quantify the effects of pattern geometry, loading direction and substrate stiffness on the strain deconcentration of thin films patterned with circular holes.

2.3 Thin stiff films with circular holes patterned in a triangular lattice

2.3.1 Simulation Model

Figure 25a illustrates a thin stiff film of thickness *t* patterned with circular holes of radius *R*, whose centers coincide with a triangle lattice of lattice spacing *L*.

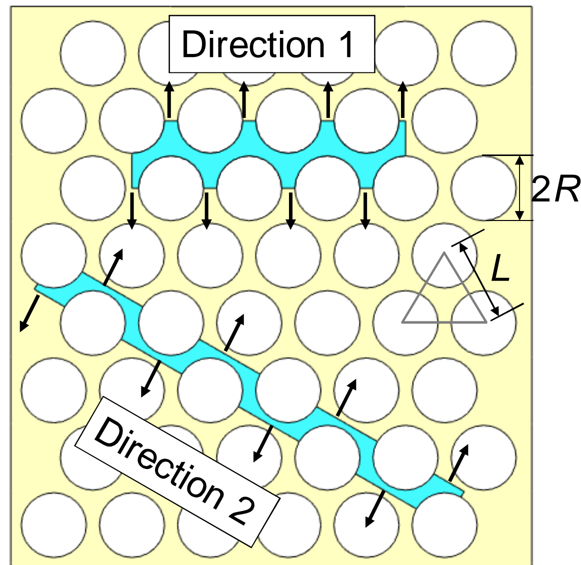

(a)

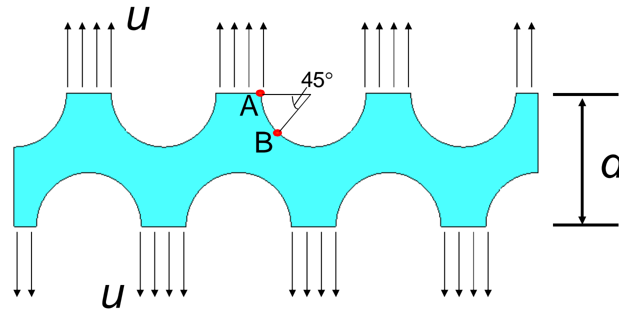

(b)

Figure 25. (a) A thin film patterned with circular holes whose centers coincide with a triangle lattice. The two shaded areas illustrate the simulation models under two representative tensile directions, respectively. (b) Schematic of the simulation model.

Due to the symmetry of the pattern, only a shaded area of the patterned thin film is simulated. The deformation of the shaded area under tension is studied in two different directions as defined in Figure 25a. These two directions represent the limiting cases of all possible tensile directions. The film ligaments along the two long parallel sides of the shaded area are subject to displacement *u* as shown in Figure 25b. To avoid confusion with the microscopic strain in the film, we call the quantity $2u/d$ the relative elongation of the film, where d is the undeformed width of the shaded area. The shaded area is meshed with three-node triangle shell elements with about 100 elements along one semi-circle hole edge and size-matching elements everywhere else. The film is modeled as a linear elastic material, with Young's modulus E=100 GPa and Poisson's ratio ν=0.3. In simulations, L/t=100, R/L=0.25, 0.35 and 0.45.

To study the effect of substrate stiffness, two deformation modes of the patterned thin stiff film under tension are studied: pure in-plane stretch and out-of-plane deflection.

These two deformation modes represent two limiting cases: a patterned thin stiff film on a rigid substrate, and a patterned thin stiff film on a sufficiently compliant substrate, respectively. To allow the out-of-plane deflection in the initially planar thin film, an imperfection of small amplitude, obtained from a buckling eigen-mode analysis, is introduced to perturb the deformation of the shaded area.

2.3.2 Results

Figure 26a shows the deformed shapes of the shaded area (*R/L*=0.45) at a relative elongation of 30%. The color contour depicts the localized strain in the FEA model.

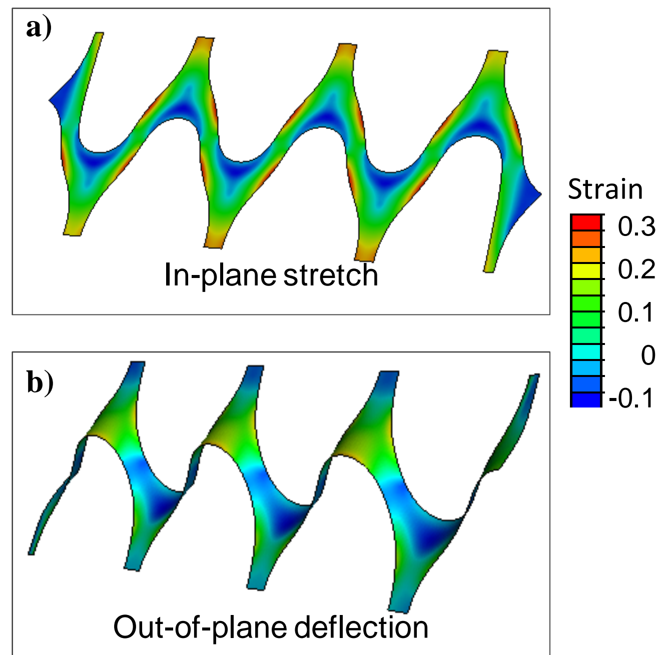

Figure 26. Deformed shapes of the shaded area in Figure 25b under a relative elongation of 30%, for two deformation modes; (a) In-plane deflections; (b) Out-of-plane deflections. Note the difference in the strain level in the film, as indicated by the color shades.

At each point in the film, the strain has two principal components, the larger of which is indicated by the shade in Figure 26. If the deformation of the film is confined in the

plane, the resulting strain can be as large as the applied elongation in certain locations near the hole edges. Note that such a strain level in the patterned film is already deconcentrated by about three-fold, compared to that in a thin blanket film with a single circular hole subject to the same elongation. Furthermore, if the patterned thin film deforms out-of-plane to accommodate the elongation, the resulting strain can be further deconcentrated. For example, at the relative elongation of 30%, the strain in majority part of the film is below 10%, with a maximum value of about 20%.

Figure 27 plots the maximum principal strain in the film, $\varepsilon_{\max}$, as a function of relative elongation, for both in-plane stretch mode and out-of-plane deflection mode. If the film deformation is confined in the plane, $\varepsilon_{\max}$ is comparable to the applied elongation, with a roughly linear dependence. If the film can deflect out-of-plane, $\varepsilon_{\max}$ is only a fraction of the applied elongation. For example, at a relative elongation of 10%, $\varepsilon_{\max}$ is only 4%, while the majority of the film experiences less than 2% tensile strain.

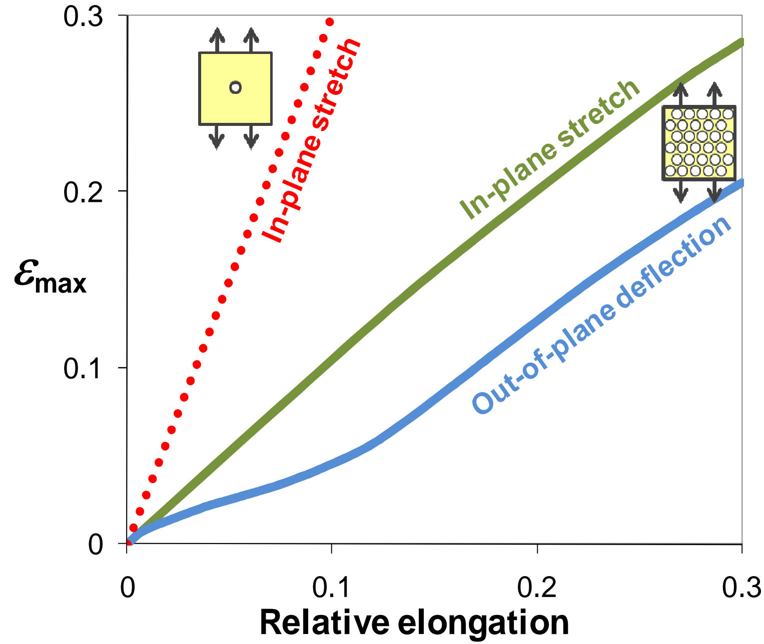

Figure 27. The maximum principal strain ε_{max} in the film as a function of relative elongation. For a blanket thin film with a single circular hole, ε_{max} is three times of the relative elongation. For a thin film patterned with an array of circular holes, in-plane stretch of the film leads to ε_{max} comparable to the relative elongation, while out-of-plane deflection of the film further deconcentrates the strain to only a fraction of the relative elongation.

To further quantify the effect of circular hole geometry and tensile direction on the strain deconcentration in the film due to out-of-plane deflection, Figure 28 plots the maximum principal strain ε_{max} as a function of relative elongation for various circular hole size/spacing ratios *R/L* and under uniaxial tension in the two directions defined in Figure 25a.

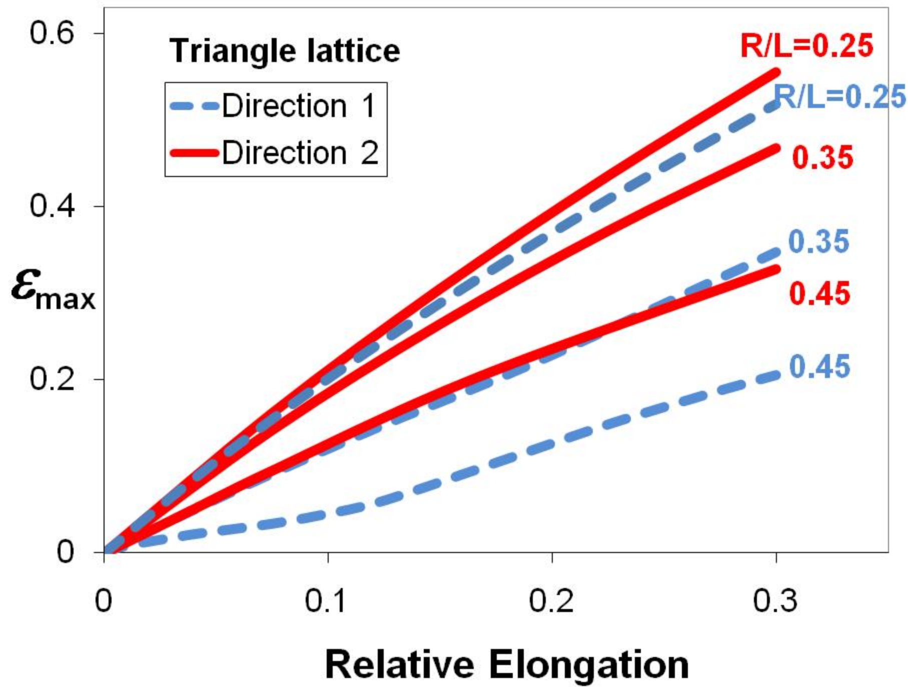

Figure 28. $\varepsilon_{\max}$ **in a thin film with circular holes patterned in a triangle lattice as a function of relative elongation, for various *R/L* ratios and two representative tensile directions.**

In all cases, $\varepsilon_{\max}$ increases monotonically as relative elongation increases. For a given relative elongation in a given tensile direction, the larger the circular hole size/spacing ratio *R/L*, the smaller $\varepsilon_{\max}$. The more substantial strain deconcentration results from the more tortuous hidden serpentines in a film with more densely packed circular holes. Furthermore, the maximum strain in the film under tension in direction 1 is smaller than that in the film under tension in direction 2, with all other parameters remaining the same. For a given *R/L,* the $\varepsilon_{\max}$ vs. relative elongation curves for tensile directions 1 and 2 define the lower and upper limits of the curves for all other possible tensile directions.

2.4 Thin stiff films with circular holes patterned in a square lattice

Figure 29a illustrates a thin stiff film of thickness *t* patterned with circular holes of radius *R*, whose centers coincide with a square lattice of lattice spacing *L*.

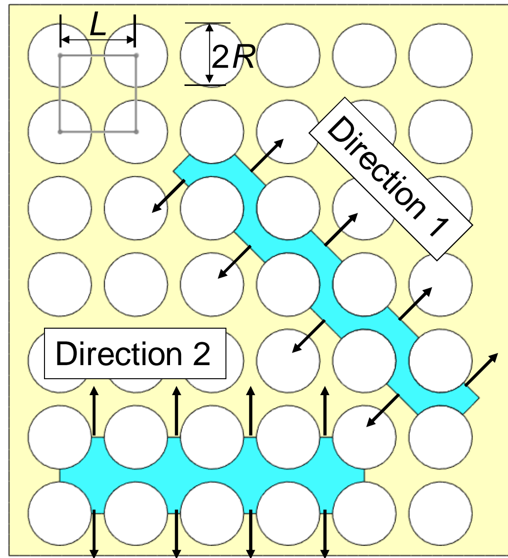

(a)

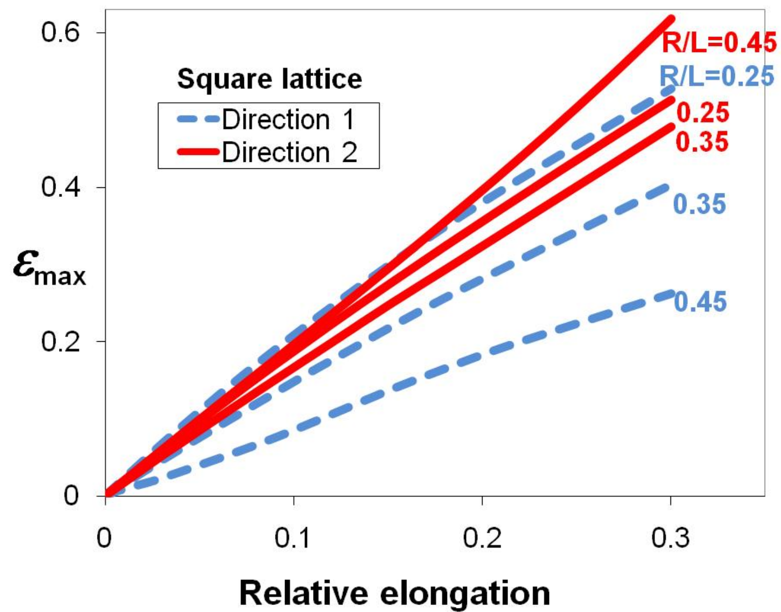

(b)

Figure 29. (a) A thin film patterned with circular holes whose centers coincide with a square lattice. The two shaded areas illustrate the simulation models under two representative tensile

directions, respectively. (b) $\varepsilon_{\max}$ as a function of relative elongation, for various *R/L* ratios and two representative tensile directions.

The simulation models are shown as the shaded areas. The resulting strains due to out-of-plane deflection when the film is under tension in two different directions as defined in Figure 29a were studied. The element type, meshing scheme and material properties used in the finite element models are the same as those defined in section 2.3.1 Simulation Model. In simulations, *L/t*=100, *R/L*=0.25, 0.35 and 0.45.

Figure 29b plots the maximum principal strain $\varepsilon_{\max}$ as a function of relative elongation, for various values of *R/L* and two tensile directions. In all cases, $\varepsilon_{\max}$ increases monotonically as relative elongation increases. Under a given relative elongation in direction 1, $\varepsilon_{\max}$ decreases as *R/L* increases. Under a given relative elongation in direction 2, $\varepsilon_{\max}$ decreases as *R/L* increases in a modest range (e.g., *R/L*<0.35), but increases if *R/L* is rather large (e.g., *R/L*=0.45). The increased strain level in a film with a large *R/L* value under tension in direction 2 can be explained as follows. As shown in the shaded area in Figure 29a, there is no hidden serpentine along the tensile direction 2 for a square hole pattern. Therefore, the elongation is accommodated by the pure stretch of the film ligaments that demarcate the circular holes. The pure stretch concentrates near the thinnest segment of the ligaments (e.g., all edges along the two long parallel sides in the shaded area of direction 2), resulting in strain higher than the applied elongation.

2.5 Discussion

In the models, the edges of the circular holes are smooth and free of defects. In practice, microfabrication procedures during film patterning inevitably introduce defects near the hole edges, such as missing grains, sharp corners, etc. When the film is subject to tension, these defects can initiate cracking in the film. Crack growth eventually leads to the failure of the whole film. In recent tensile experiments of thin gold films patterned with circular holes on elastomeric substrates, microcracks appear near the edge of some holes but the majority of the film remains intact [28]. To further understand why such patterned thin gold films can sustain large elongation without crack growth, the following simulations were performed.

A microcrack of length, a, equal to one tenth of the film thickness is introduced at the edge of a circular hole. Two representative locations and orientations of the microcrack are considered: a microcrack perpendicular to the tensile direction at point A marked in Figure 25b, and a microcrack oriented 45° from the tensile direction at point B marked in Figure 25b. Here we consider a thin film patterned with circular holes in triangle lattice and with R/L=0.45, under two deformation modes: in-plane stretch and out-of-plane deflection, respectively.

Figure 30 plots the energy release rate, G, at the microcrack tip, normalized by ER (E is the elastic modulus of Au and R is the radius of the holes), as a function of relative elongation. G is calculated by the contour integral in ABAQUS codes. Figure 31 shows a stress contour plot that focuses on the crack tip.

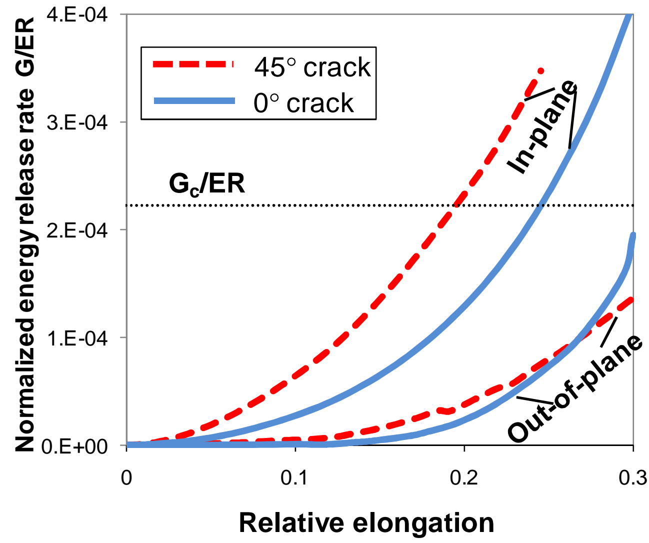

Figure 30. Normalized energy release rate *G/ER* at the microcrack tip as a function of relative elongation. Note the significant difference in the driving force of crack growth for the two deformation modes. G_c denotes the threshold value above which the microcrack grows under monotonic loading.

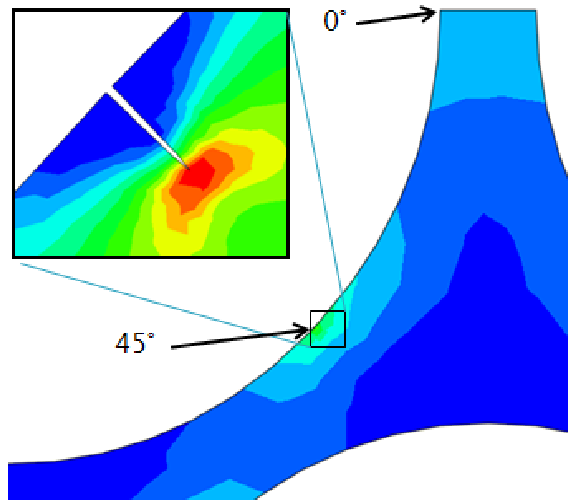

Figure 31. Crack tip stress contour

The quantity G/ER measures the driving force for crack growth. Once G reaches a critical value G_c, the microcrack grows. The larger the relative (macroscopic) elongation of the film, the larger the driving force for crack growth. Figure 30 reveals that, if the film can deflect out of plane, the energy release rate at the microcrack tip is much smaller than that due to in-plane stretch. For example, at a relative elongation of 20%, the energy release rate at a 45° crack tip due to out-of-plane deflection is only one-seventh of that due to in-plane stretch. For a thin metal film of thickness t, G_c scales with σ_Y and t, where σ_Y is the yield strength of the metal. With σ_Y = 1GPa, t = 100nm, E = 100GPa, and R = 4.5μm, we have $G_c / ER = 2.2 \times 10^{-4}$. With such a critical value, the maximum relative elongation without microcrack growth is well beyond 30% if the metal film can deflect out of plane. In contrast, if the film deformation is confined in the plane, the maximum relative elongations are only 18% and 25% to prevent microcrack growth at the two representative locations A and B, respectively.

G_c estimates the threshold of crack growth under monotonic elongation. Under cyclic loading, the fatigue crack growth threshold G_{th} is not well understood for thin metal films, but nonetheless is a fraction of G_c [7]. From Figure 30, for $G_{th} = G_c/10$, a film patterned with circular holes can still be cyclically elongated up to 16.5% without crack growth if it can deform out of plane.

2.6 Conclusion

The deconcentrated strain in thin stiff films patterned with circular holes under large elongation was studied using numerical modeling. A suitably patterned film can

elongate by deflecting out-of-plane. Consequently, large elongations induce small strains in the film. Using finite element simulations, the effects of pattern geometry, loading direction, and substrate stiffness were quantified on the strain deconcentration in these patterned films. The calculation of the driving force for crack growth near the hole edges further explains the large deformability of the patterned thin stiff films demonstrated in recent experiments. The quantitative results from this paper (e.g., Figure 28, Figure 29b, and Figure 30) can serve as guidelines in designing flexible thin films patterned with circular holes to satisfy certain deformability criterion. Furthermore, the general principle of achieving large deformability of thin stiff films by suitably patterning (e.g., circular holes) is essentially geometric, thus independent of materials and length scales. The 2D planar configuration with circular holes makes the fabrication process for this film pattern effortless when compared to previous patterning or pre-stretching efforts. Therefore, such a structural principle can be potentially applied at both device and component levels in designing architecture of flexible electronics.

Chapter 3: A Quality Map of Transfer Printing

3.1 Background

As described in the Chapter 1, transfer printing is a fabrication method used to assemble one working layer onto another in an effort to produce a multilayer functional electronic device. The mechanics of transfer printing relies on Van der Waals forces between two separate materials as they are brought together to construct layered electronic circuits [30,31]. Transfer printing primarily relies on differential adhesion for the transfer printing of a printable layer from a transfer substrate to a device substrate. Figure 32a depicts the two steps involved in transfer printing process in a simplified form. A film (or any desired printable layer) is fabricated on a transfer substrate (TS). A typical TS is a silicon wafer with a thin SiO_2 layer, while a typical film could be an Au conductor or Pn semi-conductor. The TS with printable layer attached is place over the device substrate (DS), which can be a polymer or elastomer. The two materials are brought together with the printable layer sandwiched in the middle and placed under high pressure and temperature. After a set time, the assembly is cooled down to room temperature, and the TS is peeled away completing the transfer process.

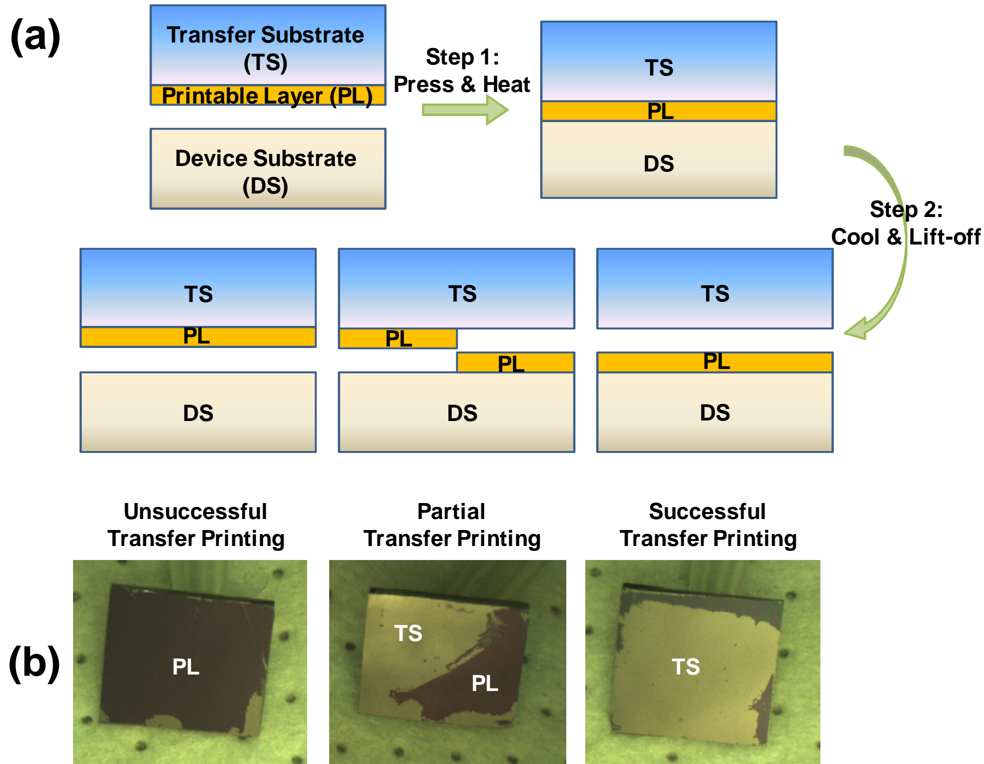

Figure 32. (a) Schematic of a transfer printing process that consists of two steps: (1) A printable layer is sandwiched in between a transfer substrate and a device substrate under pressure and elevated temperature; (2) The structure is cooled and the transfer substrate is lifted off. After such a process, the printable layer can be either successfully transferred, or partially transferred, or unsuccessfully transferred onto the device substrate. (b) (From right to left) Optical images of the silicon transfer substrates (bright region) and the remaining printable layer of poly(methyl methacrylate) (PMMA, dark region) after successful, partially successful, and unsuccessful transfer printing onto a poly(ethyleneterephthalate) (PET) device substrate, respectively. The percentage area of PMMA layer transferred onto the PET substrate are 95%, 67% and 5%, respectively, in these three cases. The size of the silicon transfer substrates are roughly 1 cm by 1 cm. The thicknesses of the PMMA layer and the PET device substrate are approximately 600 nm and 150 μm, respectively. In the successful case, the surfaces of both the printable layer and the device substrate were O_2 plasma-treated to improve adhesion; in the partial transfer printing case, only the device substrate surface was O_2 plasma-treated; while in the unsuccessful case, no surface treatment was applied.

In practice, a transfer printing process can results in successful, unsuccessful, or partial transfer printing of the printable layer onto the device substrate as shown in

Figure 32a. In the first case shown on the left, the printable layer remains adhered to the TS producing a completely unsuccessful transfer. In the second case, the printable layer is partially transferred to the DS as depicted in the middle photograph. In the final (most desirable) case, the printable layer is nearly completely transferred from the TS to the DS as seen in the right photograph.

The transfer printing process has promising features like lower working temperatures and flexible materials that may be streamlined into a roll-to-roll printing process instead of the current high temperature batch process. The batch process involves printing one layer at a time, whereas the roll-to-roll method is a continuous assembly-line where each layer is added in succession. Roll-to-roll printing promises dramatic cost reductions over the current production methods thereby making flexible electronics more attractive to the average consumer. Unlike inkjet printing[32-36] and microcontact printing[37-39], the transfer printing process is inherently compatible with nanoscale features and the resulting devices are as good as those fabricated via traditional processing methods [40].

Research has shown that Au films can be transfer printed onto substrates like PET, PMMA, and poly (4-vinylphenol) (PVP) [40]. Similarly, semi-conductors, like pentacene (Pn), have been shown to transfer print onto Au and PMMA [40]. The correct combination of multiple material layers could create an inherently flexible, fully functional circuit.

One of the problems facing transfer printing is quality. Previous transfer printing methods use the work of adhesion between an interface and the material cohesion of the materials being printed to predict successful transfer. Figure 33 shows two

different transfer printing cases. In the case on the right, the work of adhesion at the top interface (Wa) is weaker than the work of adhesion of the bottom interface (Wb). When the TS is lifted off, the top interface will break creating a successful transfer print. The case on the left shows the opposite where the weaker bonds are on the bottom interface creating an unsuccessful transfer print.

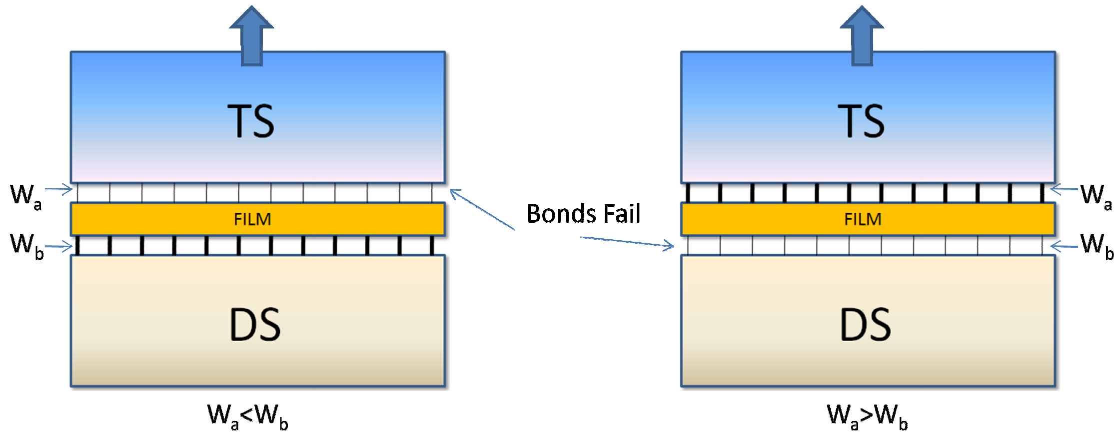

Figure 33. Differential adhesion of two different materials

A complete understanding of the transfer printing conditions governing print quality is still unknown as much of the knowledge comes from experimental trials. For example, enhanced interfacial adhesion between the printable layer and the device substrate through plasma treatment can lead to improved transfer printing quality [40]. This shows one method for controlling transfer printing quality by means of altering the adhesion between materials through surface treatment [40]. Hines et al. have conducted extensive research on the work of adhesion between different printing materials [40]. Further experiments have shown that the printing quality is also sensitive to both the detail geometry of the printable layer and the mechanical properties of the organic/inorganic hybrid materials in the transfer printing structure, with quantitative dependence remaining elusive. Another method to control transfer

printing quality uses the separation rate to control which interface will fracture as shown in Figure 34. Feng et al. have shown that damping ratios disparity between two interfaces applies different forces to each interface thereby controlling printing quality [41]. The interface between the film and the stamp is viscoelastic. When the stamp is lifted with high velocity, the force in the viscoelastic interface is high causing the interface between the film and substrate to fail. When the stamp is lifted slowly, the viscoelastic force between the film and the stamp is low allowing separation. Again, much experimentation is needed to determine the correct rates to apply to various material interfaces to obtain successful transfer prints. Furthermore, the viscoelastic interface must be easily controlled and altered to create successful transfer prints.

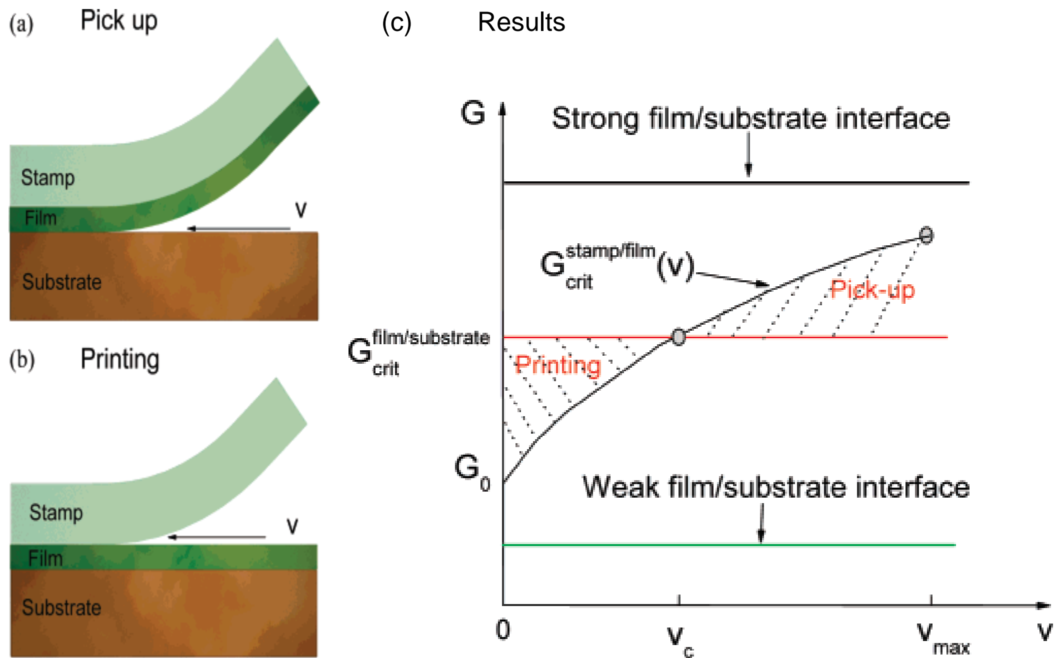

Figure 34. Kinetically controlled transfer printing a) Fast rate picks up film; b) Slow rate prints film; c) Film/substrate energy release rate vs. velocity [41]

To get a comprehensive understanding of the factors that affect transfer printing, many experiments must be conducted on a wide range of material combinations; each having different surface treatment options. This involves time intensive experimentation and limited material/treatment options. Even with the various methods to help control transfer printing, there are still difficulties to transfer print successfully. For example, it is often more difficult to transfer print onto a more compliant device substrate. Therefore, there is a need to create reliable transfer prints on materials with various mechanical properties to further the field of flexible electronics.

A successful transfer printing is essentially a well-controlled interfacial delamination process along the interface between the transfer substrate and the printable layer instead of that between the printable layer and the device substrate. During transfer printing, initial interfacial defects (e.g., cracks, voids) are highly likely to exist along the two interfaces in the tri-layer structure. Such interfacial defects may result from unmatched surface roughness or uneven registration when printing over large areas. During the lift-off step, the interfacial defects, especially those near the edges, cause stress concentration and may lead to unstable interfacial delamination. Therefore, the initial interfacial defects can have pivotal impacts on the transfer printing quality.

One method for controlling transfer printing includes the fracture mechanics of the inherent cracks along the interfaces. These cracks could be detrimental if the interfacial defects are along the interface between the printable layer and the device substrate (hereafter referred to as "the bottom interface"), but also could be beneficial if the interfacial defects are along the interface between the transfer substrate and the

printable layer (hereafter referred to as “the top interface”). In practice, initial interfacial defects exist along both interfaces, therefore it is the competition between the above two opposing defects that crucially determines the transfer printing quality. Earlier studies have shown that the substrate stiffness can substantially influence the driving force of the film-substrate interfacial delamination [29,42-47]. Most existing studies, however, deal with the interfacial delamination in a film-on-substrate bilayer. The knowledge from these studies sheds light on, but is still insufficient for, understanding the competing delamination along the two interfaces in the tri-layer transfer printing structure. While the transfer substrate is often made of SiO_2 which is stiff, the device substrate material can range from modestly compliant polymers (e.g., PET, polyimide) to extremely compliant rubber-like elastomers (e.g., PDMS). The wide range of the device substrate stiffness (e.g., from 10 GPa to 1 MPa) and the huge stiffness ratio between the transfer substrate and the device substrate (e.g., from 10 to 10^5) lead to rich characteristics of the competing delamination, which are far from well-understood.

If crack lengths and locations could be controlled between the various interfaces of a transfer printing process, the quality of a successful transfer printing could be controlled. If intentional defects could be created between normally incompatible materials, the driving force created by the intentional defects could be used to reliably create quality transfer printing. The results of this research are two-fold. First, given a set of materials with tested work of adhesion values and average crack sizes along the interfaces, this research shows the designer if successful transfer printing is likely to occur. This could save time and money spent on experimentation. Secondly, this

research shows the designer what modifications are needed to create a successful transfer print. Would increasing the defect size on one interface help, or would increasing the work of adhesion at an interface be more effective? In this regard, this research can provide instant feedback on success, and guidance on how best to adjust the results.

3.2 Methods

FEA modeling with ABAQUS software was used to determine the effects of defects (cracks) ideally located along the interface between two layers as the TS is lifted off of the assembly. Figure 35 shows the location of the two cracks and the associated geometric dimensions. The length of the top crack, L_t, and the length of the bottom crack, L_b, were both normalized with respect to the height of the film, h, during the analysis. The lengths and heights of the substrates were fixed to 1000 times the height of the film (h), while the crack lengths never exceeded 4% of the length of the film/substrate interface. In real transfer printing processes, the thickness of the printable layer is about 100 *nm* while the substrates are on the order of 100s μm.

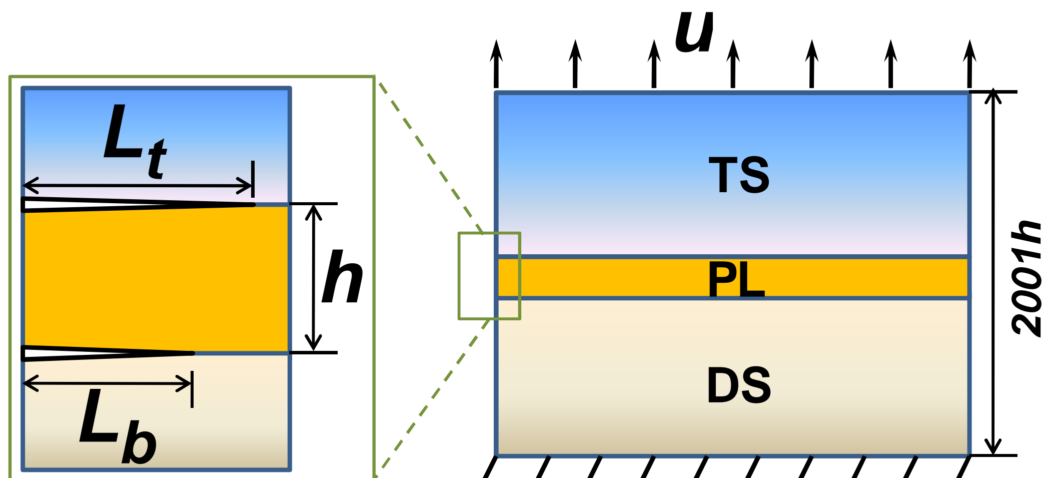

Figure 35. Schematic of the interface cracks in the transfer printing computational model (not in scale).

The defects (cracks) were controlled by setting L_t and varying L_b in multiple models. Similarly, another set of models were created with a different L_t value resulting in a complete matrix of defect sizes. During the analysis, the driving force for the interfacial crack at the top interface (or bottom interface) to propagate is quantified by the energy release rate (G) at the crack tip G_t (or G_b). The energy release rates of both cracks were analyzed using the J-integral calculated in the ABAQUS program.

If the driving force for the top interfacial crack, G_t , is greater than the interfacial adhesion energy between the transfer substrate and the printable layer, G_t^c , delamination along the top interface occurs. Similarly, if G_b is greater than G_b^c , the interfacial adhesion energy between the printable layer and the device substrate, delamination along the bottom interface occurs. In practice the lift-off step is not force-controlled; the competing delamination is thus governed by the *differential* driving force for crack propagation at the two interfaces, rather than their absolute values. It can be presumed that the two interfaces have different interfacial work of adhesion values. Therefore, much of the analysis will be based on ratios between the two interfacial works of adhesion and the energy release rates. For a given combination of the interfacial adhesion energies in a transfer printing structure (i.e., G_t^c and G_b^c), if

$$G_t / G_b > G_t^c / G_b^c , \tag{1}$$

the top interfacial crack will propagate and initiate the delamination along the top interface. Alternatively, if

$$G_t / G_b < G_t^c / G_b^c , \tag{2}$$

the bottom interfacial crack will propagate and initiate the delamination along the bottom interface. In Eqs. (1) and (2), the left-hand side denotes the external driving force for delamination, and the right-hand side represents the materials properties of the transfer printing structure. As will be shown later on, once a delamination starts to propagate along an interface, the driving force keeps increasing as the crack advances, leading to a steady delamination along that interface until final separation. This said, the transfer printing quality can then be characterized by the differential driving force of interfacial delamination in the following way:

$$G_t / G_b > G_t^c / G_b^c \rightarrow \text{Successful transfer printing, and}$$

$$G_t / G_b < G_t^c / G_b^c \rightarrow \text{Unsuccessful transfer printing.}$$

For example, for a transfer printing assembly with equal interfacial adhesion energy ($G_t^c / G_b^c = 1$), the transfer printing will be successful if $G_t / G_b > 1$, and otherwise unsuccessful if $G_t / G_b < 1$. In practice, a steady delamination along one interface could give way to the fracture of the printable layer itself and the subsequent delamination along another interface, leading to the partial transfer printing. The fracture of the printable layer may result from the stress concentration near its own initial imperfections (e.g., microvoids, microcracks). The study of "partial" transfers is beyond the scope of this report.

Three-node and four-node plane strain elements were used in the FEA analysis since it modeled a thin blanket printable layer. Figure 36 shows the full FEA model which is too large to see the thin film region. Figure 37 shows a close-up image of the regions near the crack tips. Large three-node triangular elements are used far away

from the crack region, and the mesh density increases closer to the film. The film is composed of four-node elements to increase the fidelity of the results. Extremely dense mesh regions were created around the crack tips. The uniform nature of the mesh patterned allowed uniform contour integral regions to be created for the J-integral analysis. For each crack tip, 20 layers of elements emerge from each side allowing for 20 contour integrals. Therefore, the mesh size for most contour regions was h/20. As the crack lengths become very short (i.e. < h), the contour regions and meshes were scaled down to match the crack length.

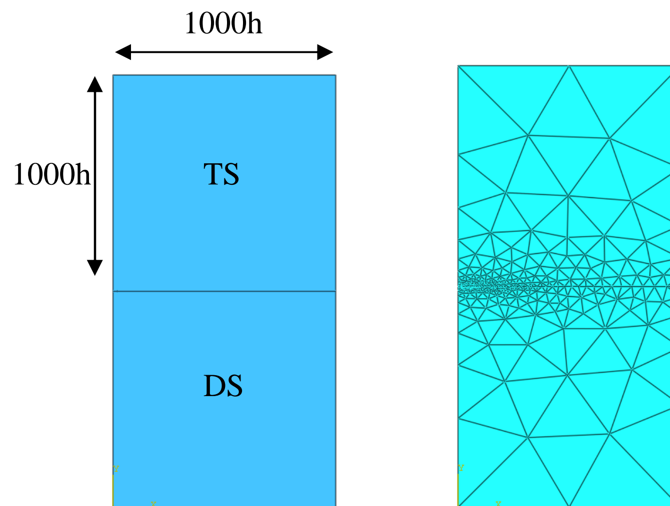

Figure 36. Transfer printing FEA model mesh size

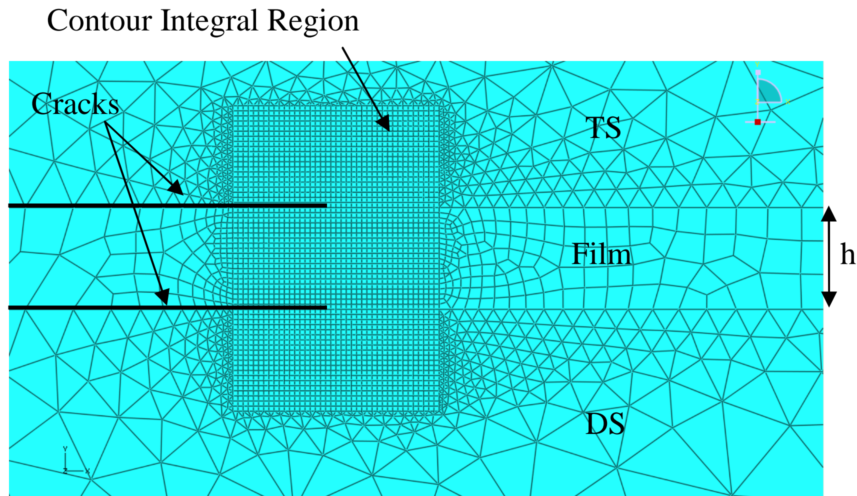

Figure 37. Transfer printing FEA crack mesh size

The modeling was first performed to characterize the effect of transfer printing an Au film from a SiO_2 transfer substrate to a PET device substrate. Au was given an elastic modulus of 78 GPa with a Poisson's ratio of 0.44, while the PET and SiO_2 were given elastic moduli of 2.6 GPa and 71 GPa and Poisson's ratios of 0.37 and 0.16 respectively. All material was assumed to be linear elastic and isotropic with respect to their material properties. The vertical displacement is set to be zero along the bottom surface of the device substrate and set to be u along the top surface of the transfer substrate. This simulates the lift-off step of the transfer printing process. The quantity $\varepsilon = u / 2001h$ will be called the applied strain.

Three more defect matrices were created using different DS material properties. The PET was replaced with PDMS, while the Au film and SiO_2 transfer substrate remained fixed. Because PDMS can have many different mechanical properties based on the degree of cross-linking in the polymer, PDMS was modeled with an elastic modulus of 1, 10, and 100 MPa and a Poisson's ratio of 0.5. This gave a range starting with an extremely compliant to a moderately compliant device substrate.

The energy release rates of the two interfacial cracks are calculated by the contour integral in the finite element code ABAQUS. In describing the simulation results, the following dimensionless groups were used: $G_t / E_{PL}\varepsilon^2 h$, $G_b / E_{PL}\varepsilon^2 h$, G_t / G_b, L_t / h and L_b / h, which denote the normalized driving force of delamination along the top interface, the normalized driving force of delamination along the bottom interface, the differential driving force of delamination, the normalized length of the top interfacial crack and the normalized length of the bottom interfacial crack, respectively.

3.3 Results

First, the two limiting cases are considered where an interfacial edge crack exists only in one of the two interfaces in a transfer printing structure. Figure 38 plots the normalized energy release rate $G_b / E_{PL}\varepsilon^2 h$ (or $G_t / E_{PL}\varepsilon^2 h$) of an edge crack along the bottom (or top) interface as a function of normalized crack length L_b / h (or L_t / h) for various device substrate materials. Here L_t / h=0 if $L_b / h \neq 0$ (all solid lines), or L_b / h=0 if $L_t / h \neq 0$ (all dash lines). In both cases, for a given device substrate material (i.e., E_{DS} and ν_{DS}), the energy release rate at the interfacial crack tip increases monotonically as the crack length increases, and saturates when the crack length reaches a few hundred times the thickness of the printable layer. As the device substrate stiffness decreases, the energy release rate drops considerably. This can be understood as follows: For a given applied strain ε as defined earlier, a more compliant the device substrate (i.e., smaller E_{DS}) accommodates more of the applied strain through the bulk deformation of the device substrate; thus the driving force for

interfacial crack propagation is smaller. The comparison between the two cases shows that if the device substrate is sufficiently stiff (e.g., E_{DS} >100 MPa), the difference between the energy release rate of a top interfacial crack and that of a bottom interfacial crack of the same length is negligible. However, if the device substrate is compliant (e.g., E_{DS} =10 MPa or 1 MPa), the energy release rate of a top interfacial crack is much smaller than that of a bottom interfacial crack of the same length when the crack is short (e.g., L_t/h (or L_b/h) < 20). Such a difference diminishes and becomes negligible when the crack is significantly long (e.g., L_t/h (or L_b/h) > 100). The trend can be explained by the increased deformation accommodated by the bulk device substrate as its stiffness decreases. As the bottom crack gets smaller, there is less of a free edge capable of accommodating the needed strain which leads to increased stress. So instead of the energy release rate going down to zero for the compliant materials, it remains flatter.

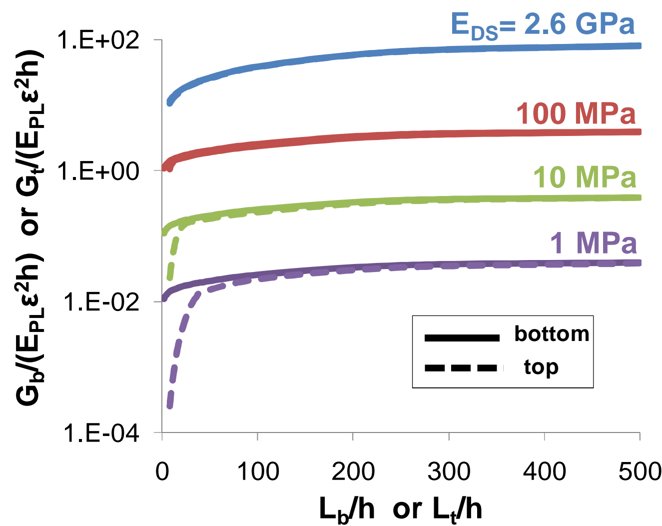

Figure 38. Solid lines: normalized energy release rate $G_b / E_{PL}\varepsilon^2 h$ of an edge crack at the bottom interface as a function of normalized crack length L_b / h, for various device substrate stiffness. No crack

exists at the top interface; Dashed lines: $G_t / E_{PL}\varepsilon^2 h$ as a function of L_t / h for an edge crack at the top interface, for various device substrate stiffness. No crack exists at the bottom interface.

Next, the competing interfacial delamination during lift-off is analyzed by determining the driving force for the propagation of interfacial edge cracks of various lengths along the two interfaces in a transfer printing structure. Given the monotonic increase of the energy release rate of the interfacial cracks with increasing crack length (as shown above), we focus hereafter on the competing interfacial delamination at the early stage of lift-off (i.e., smaller L_b / h and L_t / h).

Figure 39 plots the normalized energy release rates $G_b / E_{PL}\varepsilon^2 h$ of an edge crack at the bottom interface and $G_t / E_{PL}\varepsilon^2 h$ of an edge crack at the top interface as functions of the normalized bottom interfacial crack length L_b / h for various top interfacial crack lengths $(L_t / h = 4, 20, 40)$ and various device substrate materials ($E_{DS} = 2.6\,GPa, 100\,MPa, 10\,MPa, 1\,MPa$). Take the case of $E_{DS} = 2.6\,GPa$ as an example. For a given length of the edge crack at the top interface (e.g., $L_t / h = 20$), the energy release rate of the bottom interfacial crack $G_b / E_{PL}\varepsilon^2 h$ remains nearly zero while that of the top interfacial crack $G_t / E_{PL}\varepsilon^2 h$ remains nearly a constant if the length of the bottom interfacial crack is much smaller than that of the top interfacial crack (i.e., $L_b / h << L_t / h$). As L_b / h becomes comparable to L_t / h, $G_b / E_{PL}\varepsilon^2 h$ rapidly ramps up while $G_t / E_{PL}\varepsilon^2 h$ abruptly drops down. When L_b / h becomes slightly greater than L_t / h, $G_t / E_{PL}\varepsilon^2 h$ becomes negligible while $G_b / E_{PL}\varepsilon^2 h$ converges into the curve corresponding to $E_{DS} = 2.6\,Gpa$ in Figure 38, regardless of

the top interface crack length. As the device substrate stiffness decreases, the overall level of the energy release rates for both interfacial cracks decreases for a given applied strain ε, and the ramping up of $G_b / E_{PL}\varepsilon^2 h$ and the dropping down of $G_t / E_{PL}\varepsilon^2 h$ as L_b / h increases also becomes more gradual. It is interesting to note that originally $G_b / E_{PL}\varepsilon^2 h$ tends to zero for $L_t / h = 4$ when $E_{DS} = 2.6GPa$, but it starts to level off for more compliant materials due to the increased deformations and stresses around the cracks.

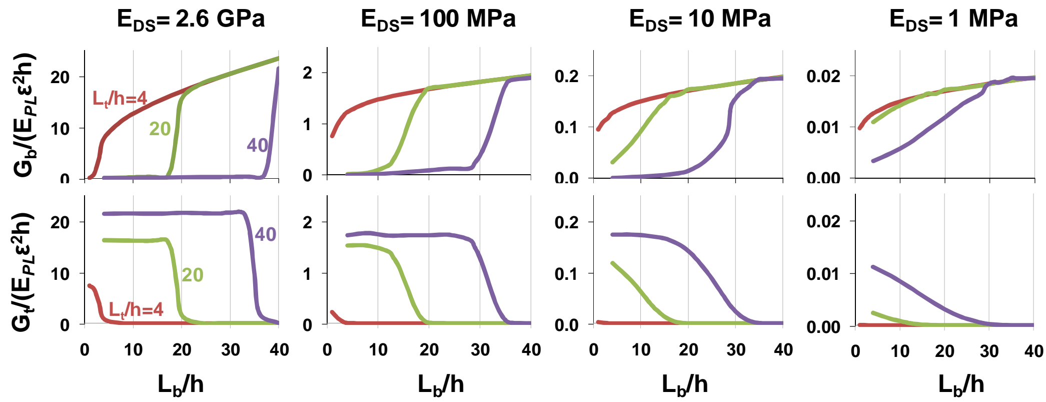

Figure 39. Normalized energy release rates $G_b / E_{PL}\varepsilon^2 h$ of an edge crack at the bottom interface and $G_t / E_{PL}\varepsilon^2 h$ of an edge crack at the top interface as functions of the normalized bottom interfacial crack length L_b / h for various top interfacial crack lengths and device substrate materials.

The figures above show a fairly consistent trend, however, it is hard to understand the interplay between the competing cracks. The graphs showing a 2.6 GPa DS depict an extremely sharp rise (or fall) in energy release rate, while the more compliant material have more gradual slopes. It will be shown later that the ratios of the energy release rates are a more useful tool for predicting failure.

To further elucidate the interplay between the two interfacial cracks shown in Figure 39, Figure 40 plots the Von Mises stress field near the interfacial cracks for various

crack length combinations (i.e., L_t/h=20 and L_b/h=4, 8, 12, 16, 20) under the same applied strain. Here $E_{DS} = 2.6\,GPa$. If $L_b/h << L_t/h$, the stress concentration only occurs near the tip of the top interfacial crack, while the low stress level near the tip of the bottom interfacial crack is comparable to that in the bulk substrates. As L_b/h increases (but is still smaller than L_t/h), the stress fields near two crack tips remains approximately unchanged due to the shielding effect of the long top interfacial crack. When $L_b/h = L_t/h$, stress concentration occurs at both crack tips. If $L_b/h >> L_t/h$ (not shown in Figure 40), the top interfacial crack, in turn, is shielded by the long bottom interfacial crack, leading to high stress concentration near the bottom crack tip but low stress level near the top crack tip. Since the energy release rate scales with the square of the overall stress level near the crack tip, the trend of change in $G_b/E_{PL}\varepsilon^2 h$ and $G_t/E_{PL}\varepsilon^2 h$ as L_b/h and L_t/h vary, as shown in Figure 39, can be readily understood.

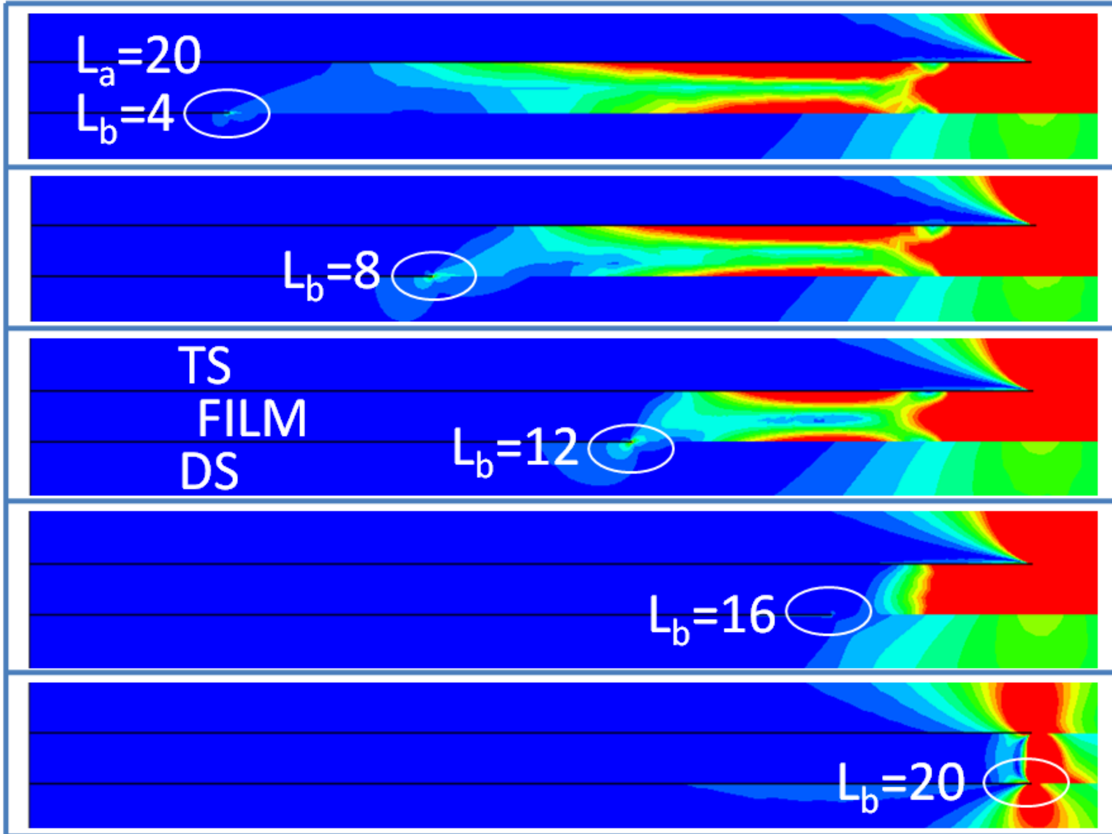

Figure 40. Von Mises stress field near the interfacial cracks for various crack length combinations. Here $E_{DS} = 2.6\,GPa$, $L_t/h = 20$. Color shades: red indicates high stress level and blue indicates low stress level. When $L_b/h < L_t/h$, the high stress concentration near the tip of the top interfacial crack remains approximately unchanged, while the stress level near the tip of the bottom interfacial crack is low. When $L_b/h = L_t/h$, stress concentration occurs at both crack tips. Note the maximum shielding effect of the top interfacial crack to the bottom interfacial crack when $L_b/h = 16$.

Figure 40 shows the energy release rate (hence stress) around the bottom crack is always less than the top crack until the bottom crack reaches a length of 20. In the top three contour plots, bending stresses in the film are transferred to small stress concentration around the bottom crack, highlighted with a white circle. In the fourth plot from the top, the stresses on the film change from a bending pattern, noted by the high stress regions on the top and bottom of the film, to a shear pattern, noted by the

vertical stress wave front. The high stress region of the shear stress does not reach the bottom crack at all. The bottom crack experiences less stress in this configuration than in all the other plots. The decrease in stress around the bottom crack while the stress around the top crack remains the same suggests a spike in energy release rate when the bottom crack is 4 units below the top crack length.

3.4 Discussion

As discussed above, the transfer printing process is governed by the competing interfacial delamination as determined by Eqs. 1 and 2. Based on the energy release rate of each interfacial crack, Figure 41 plots G_t / G_b as a function of L_b / h for various device substrates. Here L_t / h =20. For a given combination of interfacial crack lengths (i.e., L_b / h and L_t / h), the differential driving force of interfacial delamination increases as the stiffness of the device substrate increases. The physical significance of Figure 41 can be further explained as follows, using the case of equal interfacial adhesion energy ($G_t^c / G_b^c = 1$) as an example. The G_t / G_b - L_b / h curve for $E_{DS} = 2.6\,GPa$ crosses the line of G_t / G_b =1 at $L_b / h = 18.9$. That is, for a given edge crack of length 20*h* along the top interface, there is a critical length of an edge crack along the bottom interface $L_b^c = 18.9h$, shorter than which transfer printing is successful (i.e., $G_t / G_b > G_t^c / G_b^c$) and longer than which transfer printing is unsuccessful (i.e., $G_t / G_b < G_t^c / G_b^c$). Similarly, as shown in Figure 41, L_b^c = 15.3*h* and 8.5*h* for $E_{DS} = 100 MPa$ and 10 *MPa*, respectively. In practice, the interfacial adhesion of the top and the bottom interfaces can be considerably different (e.g.,

plasma treatment of the bottom interface can lead to significant decrease of G_t^c / G_b^c).

Values of L_b^c in those cases can be determined from Figure 41 in the similar manner. For example, for $E_{DS} = 10\,MPa$, L_b^c increases from 8.5*h* to 14.8*h* if G_t^c / G_b^c decreases from 1 to 0.1; meaning, an enhanced interfacial adhesion along the bottom interface results in a transfer printing process that is more tolerant of the defects at the bottom interface.

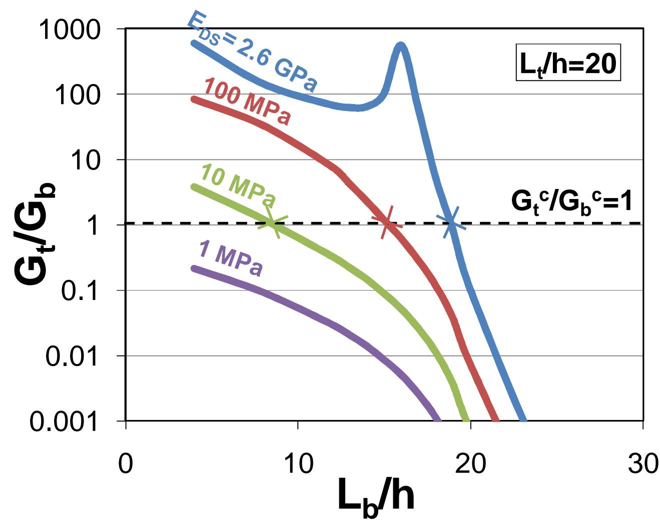

Figure 41. G_t / G_b **as a function of** L_b / h **for various device substrates. Here** L_t / h**=20. The dashed line denotes the case of equal interfacial adhesion energy** $G_t^c / G_b^c = 1$.

The spike in the energy release rate ratio curve predicted by the stress plot in Figure 40 is shown in the EDS=2.6 GPa curve in Figure 41. When a more compliant device substrate was modeled, decreases in stress around the bottom crack and the sharp peaks in the energy release rate ratios were not observed as shown in Figure 41. Furthermore, the plot shows the trend of decreasing energy release rate ratios as the stiffness of the DS decreases. The shifting of the curve down is not ideal for successful transfer prints. Lowering the curves essentially increases the energy

release rate for the bottom crack creating the potential for cracking along the bottom interface leading to an unsuccessful transfer print.

The above plots only provide meaningful results for situations where the top crack is fixed at a length ratio (L_a/h) of 20. To obtain a more universal map, multiple plots like the one shown in Figure 41 were combined into a contour line plot to create a printing map for the SiO2-Au-PET system. Each line depicts a constant energy release rate value for multiple crack length cases similar to the one shown in Figure 41.

Figure 42 shows the map for this system with the bottom crack length plotted on the y-axis and the top crack length plotted on the x-axis. Five constant energy release rate ratio lines were plotted for this combination. The region between the $1*10^{-2}$ and $1*10^{2}$ energy release rate lines is extremely narrow. Therefore, changing the crack sizes can have a major effect on the quality of the transfer printing while changing the interfacial adhesion energy will only have a small effect. For an interfacial work of adhesion line equal to one of the energy release rate ratio lines, any combination of crack lengths to the right will create a successful print while any to the left will create an unsuccessful print.

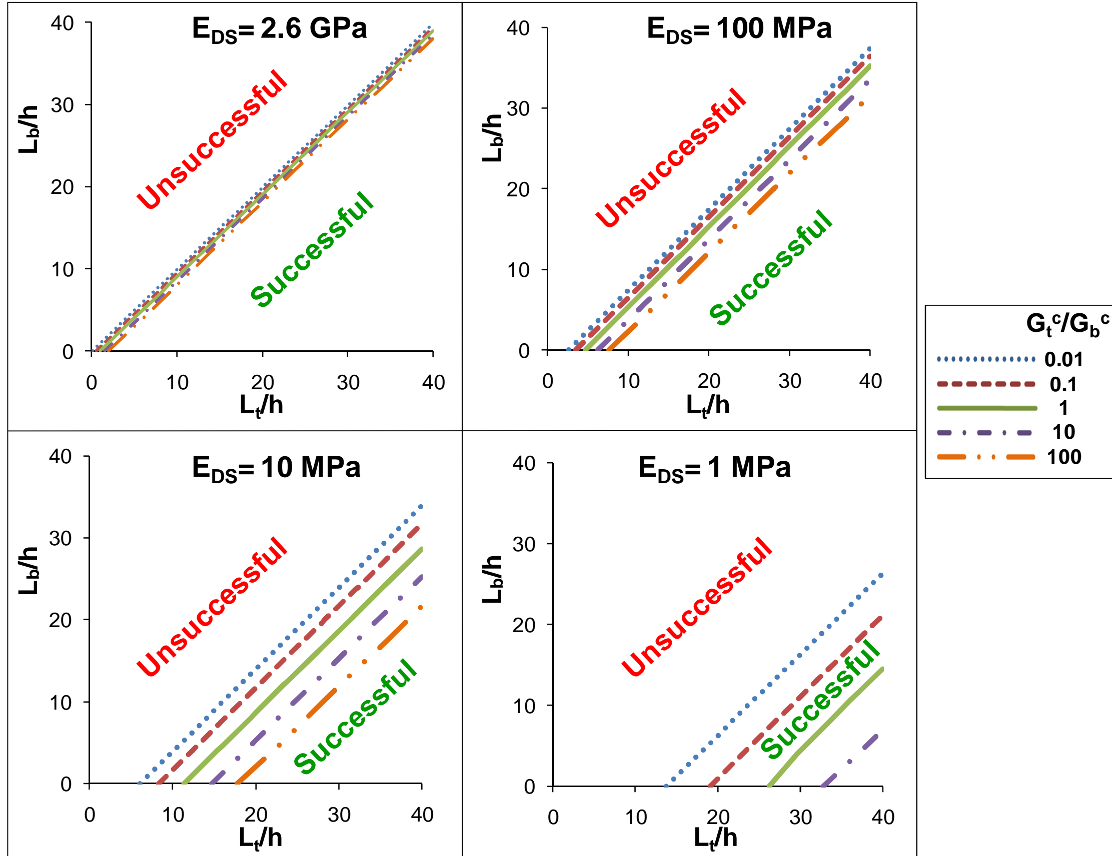

Figure 42. A quality map of transfer printing. Each curve defines a boundary line in the space of L_b / h and L_t / h, for a given E_{DS} and G_t^c / G_b^c, below which transfer printing is expected to be successful and otherwise unsuccessful.

The upper left graph in Figure 42 shows the quality printing map for PET while the other three graphs show the quality printing maps for PDMS with varying stiffnesses. These plots illustrate the effect the DS has on the printing quality map. As the DS gets more compliant compared to the constant film and TS stiffness, it becomes more difficult to produce quality transfer printing. Not only do the constant energy release rate ratio lines shift to the lower right, the width between the lines increases. The increased width between the constant energy release rate lines implies that alteration

of the interfacial adhesion energy can have a greater effect on the printing quality as opposed to the PET system shown above.

When a very compliant PDMS (1 MPa) is used as the DS, the top crack must be about 7 times longer than the bottom crack to create a successful transfer print when L_b/h=4 while assuming equal interfacial adhesion energies. Transfer printing onto PDMS with a stiffness of 10 MPa gives slightly more reasonable results. Crack lengths of 4 times the average top interface crack length must be seen along the bottom interface to create a successful transfer when L_b/h=4. Finally, as the stiffness of the PDMS increases to 100 MPa, the printing map begins to look more like the PET substrate map.

The significance and implication of the quality map of transfer printing depicted in the figures above can be further delineated as follows.

(1) *The transfer printing quality is determined not only by the relative interfacial adhesion* G_t^c / G_b^c *in the tri-layer transfer printing structure, but also by the defects (e.g., cracks) along the two interfaces.* In certain cases, the transfer printing quality could be dominated by the interplay between the interfacial defects. For example, for a stiff device substrate (e.g., E_{DS} =2.6*GPa)*, all boundary lines ranging from G_t^c / G_b^c = 0.01 to 100 form a narrow band width. In other words, even a huge difference in the relative interfacial adhesion leads to an insignificant change in the transfer printing quality. In contrast, the quality of transfer printing is rather dominated by the relative length of the interfacial cracks when a stiff device substrate is used.

(2) *Transfer printing onto a compliant device substrate is more challenging than onto a stiff device substrate*. This is evident as the decreasing successful transfer printing region in the space of L_b / h and L_t / h as the device substrate becomes more compliant. Such a prediction in general agrees with the experimental observations [40]. Also evident is that for more compliant device substrates, the transfer printing quality can be further tailored by improving the interfacial adhesion along the bottom interface or worsening that along the top interface as indicated by the increasing spacing between the boundary lines in the space of L_b / h and L_t / h for various G_t^c / G_b^c

.

(3) *Transfer printing quality can be enhanced by controlling the interfacial defects.* All boundary lines show a monotonic increase trend in the space of L_b / h - L_t / h which suggests a practical strategy to improve the transfer printing quality by introducing initial defects along the top interface of a transfer printing structure. This can be achieved by controlled surface treatment of the transfer substrate in the regions to be registered to the edges of the printable layers. The quality maps offer a quantitative guideline for the size of the top interfacial crack to be introduced to achieve a certain tolerance of the natural interfacial defects along the bottom interface in a transfer printing process. Conversely, transfer printing quality can also be improved by reducing the size of possible interfacial defects along the bottom interface (e.g., via minimizing the surface roughness of the device substrate). In this regard, the quality maps shed light on the desired device substrate surface roughness to control the interfacial crack size along the bottom interface.

3.5 Concluding Remarks

From the results, transfer printing quality maps can be created for any material as long as the material properties can be adequately modeled using FEA. Designers of flexible electronics can benefit from such material maps when choosing materials and fabrication processes. This could decrease the design and experimentation time needed to develop the transfer printing technology.

Certain assumptions were made in the FEA modeling to simplify the process. The models did not take into account stresses created by thermal mismatch. To get a more detailed picture of the stresses created at defect locations, the thermal strains created during transfer printing can be modeled. Secondly, the models were treated as though the transfer print was either successful or unsuccessful. In reality, partial adhesion and material cohesion can also be considered.

Finally, further investigations into creating defects along interfaces can be studied. This research presented a possible method for controlling transfer printing quality through defects. For this idea to become a reality, manufacturing techniques must be designed to intentionally apply defects along a specified interface. Furthermore, much experimentation is needed to verify the FEA modeling.

This chapter presented a method to control transfer printing quality through strategic defect placement. Intentional defects can be used as a tool to control successful transfer printing. FEA modeling can show where cracks need to be located to create high energy release rates. Combining these plots can create a transfer printing quality map that can be used to strategically evoke defects in one interface. Multiple transfer printing quality maps show trends towards increased difficulty when attempting to

transfer print onto extremely compliant substrates. However, properly sized and placed defects have been shown through modeling to increase the ability to transfer print onto compliant substrates.

Chapter 4: Failure Mechanisms of Barrier Layers for Flexible Electronics

4.1 Background

As noted in the introduction, flexible electronics are much more vulnerable to the attack of environmental moisture and oxygen than their microelectronics counterpart. The functional layers of flexible electronic devices (e.g., the light emitting layer in OLEDs) are vulnerable to oxidation and corrosion when exposed to natural environments containing water vapor. Flexible electronics often use organic layers (e.g., PET) as substrates, which is much more susceptible to water vapor permeation than the conventional substrate materials (e.g., Si) [48]. Water permeation through the organic layers of flexible electronics has been shown to significantly decrease the lifespan of such components [48-50]. For example, when exposed to ambient environment, unprotected bare OLEDs form dark spots in their organic electroluminescent layers, leading to a service life of only several days (as shown in Figure 43).

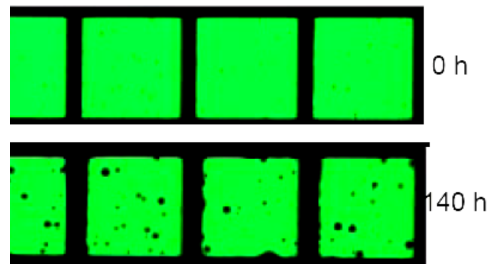

Figure 43. Top: Picture of a set of OLED pixels as-made; Bottom: After only 140 hours of operation, dark spots appear in the OLED pixels. The size of the dark spots continuously grow with time. [51]

The vulnerability of flexible devices to moisture and oxygen motivates the development of high performance permeation barriers. Figure 44 shows the

performance of various barrier techniques for OLED devices. The most effective method involves a glass-to-glass barrier with a desiccant which degrades 50% in a year, while the OLED encapsulated in plastic degrades 50% in 100 days.

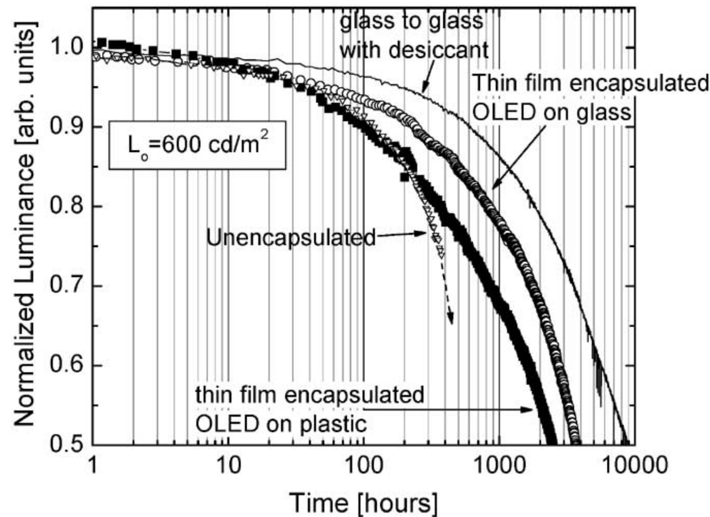

Figure 44. OLED luminance versus time using different barrier layers technology [48]

While glass has been shown to be highly effective as a permeation barrier material, it is brittle and easy to fracture at small strains. The large and cyclic deformation of flexible devices requires permeation barriers of both high performance and sufficient deformability. To this end, hybrid permeation barriers have been proposed to impede the water permeation into flexible electronic circuits while remaining flexible by stacking thin (~10 nm) rigid inorganic layers alternating with compliant organic layers. The stiff inorganic layer is typically made of oxides (e.g., AlO_x) whose water vapor transmission rate is extremely low. The organic layers have higher water vapor transmission rates but provide overall flexibility to the multilayer permeation barrier. Each inorganic/organic pair is called a dyad and multiple dyads form a permeation barrier as shown in Figure 45.

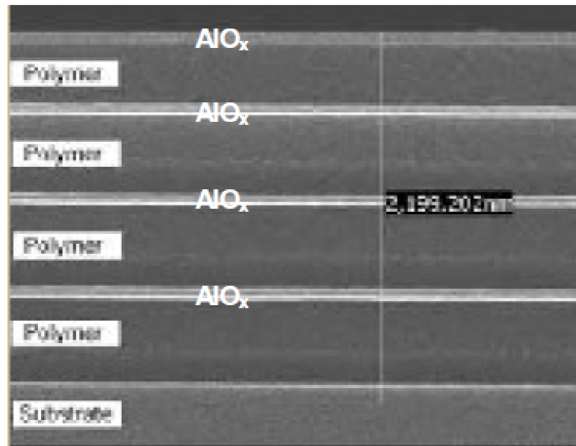

Figure 45. Hybrid barrier layer made from multiple dyads of inorganic/organic layers (Vitex Systems, Inc.)

The barrier mechanism of the hybrid multilayer permeation barriers can be explained as follows.

Permeation through a single layer of inorganic barrier

Thin film permeation barriers have traditionally been made of Al or Al or Si oxides. Bulk oxides and Al are effectively impermeable to moisture and oxygen. But, traditional thin film single barrier layers provide at best only two to three orders of magnitude improvement over the permeation rates of polymer substrates. Such a limited barrier performance results from the permeation through the defects in the barrier film rather than the bulk of the film. The source of defect-driven permeation has been primarily attributed to pinhole defects. Some secondary mechanisms include low density and/or surface roughness of the inorganic layers. Figure 46a illustrates the vapor diffusion path through a single pair of polymer/Al_2O_3 layers (referred to as a “dyad” hereafter). The flux through the pinholes serves as point sources of the vapor permeation into the adjacent downstream polymer layer.

Permeation through multilayer barriers

In a multilayer barrier, the polymer layers ‘‘decouple’’ the defects in the inorganic oxide layers. Given the concentrated vapor permeation through the defects in each individual inorganic layer (Figure 46a), the vapors need to diffuse in the polymer layers to reach the defect locations in the next downstream oxide layer. When the defects in adjacent oxide layers are widely spaced, the vapor diffusion in the polymer layers is preferably along the in-plane directions, rather than along the thickness direction. As a result, the effective vapor diffusion path through the multilayer barrier will be much longer than the thickness of the multilayer stack, as illustrated in Figure 46b. Such long and meandering diffusion paths cause a pronounced increase in lag time of the vapor permeation, resulting in a significant enhancement of barrier performance.

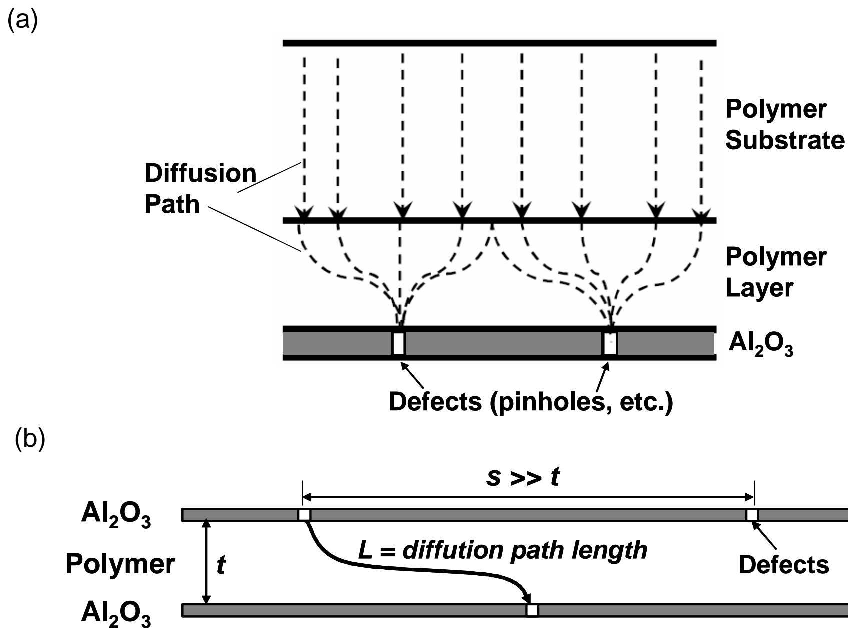

Figure 46. (a) Vapor diffusion paths through the defects in the Al_2O_3 layer of a dyad. (b) The multilayer geometry provides an effective diffusion path much longer than the polymer layer thickness when the defects in adjacent Al_2O_3 layers are widely spaced [52].

Under large deformation, the brittle inorganic layers in the hybrid multilayer permeation barriers may fracture, for example, forming cracks or delaminating from the organic layers. Such defects are expected to severely decrease the performance of the permeation barriers by substantially increasing the water vapor permeation source, as illustrated in Fig. 50.

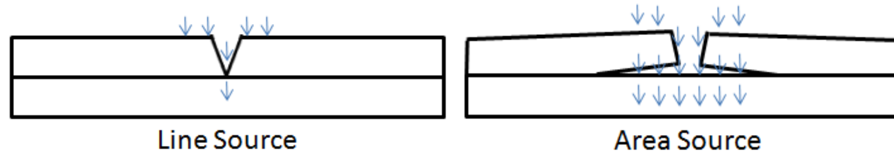

Figure 47. A channel crack creates a line source where the water vapor could bond to the Al_2O_3 while debonding creates an area where water could easily pass through the organic layer.

So far, the study of the failure mechanism of hybrid multilayer permeation barriers is rather limited. To the best of our knowledge, there is only one paper [53] in which the cracking of the inorganic layers in multilayer permeation barriers is studied.

Figure 47 summarizes the findings of that paper, which shed light on optimizing the organic layer thickness to increase the stretchability of the multilayer permeation barriers [53]. Three different cracking modes were analyzed. Starting on the left, a crack through all three layers had the lowest critical strain. As the organic layer increased in thickness, the channel crack on the top inorganic layer combined with a tunneling crack through the bottom inorganic layer created the next highest critical strain. Finally, when the organic layer is equal to or thicker than the inorganic layer, only a channel crack in the top inorganic layer forms at the lowest critical strain. Since most organic layers are thicker than the inorganic layers, a channel crack in the top inorganic layer is the most probable crack propagation mode for the tensile stretching of this barrier layer.

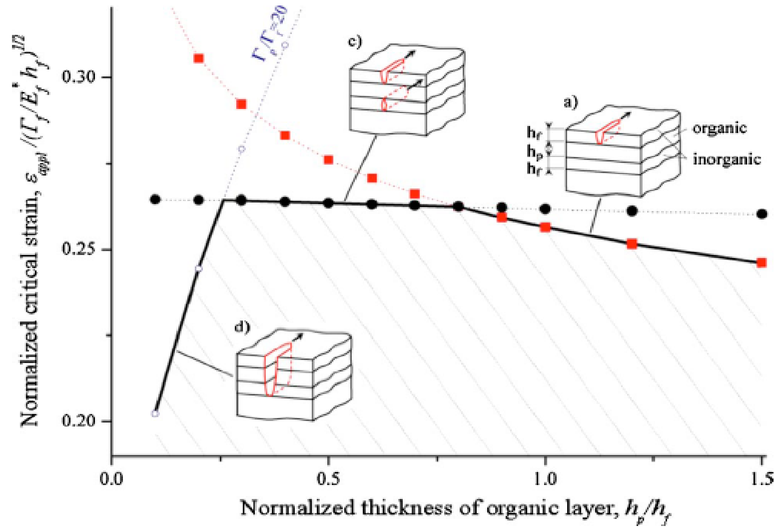

Figure 48. Crack propagation mode analysis in barrier layers [53]

The above research only considered the cracking of the inorganic layers in the multilayer barriers, but not the delamination of inorganic layers from the organic layers. In practice, both failure mechanisms may exist. Furthermore, as shown in Fig. 50, a delaminated area between the inorganic and organic layer may lead to much more severe damage to the barrier performance by offering an area source of water vapor. Above said, it is highly desired to systematically study the failure mechanisms of the hybrid multilayer permeation barriers, based on which a better design of the permeation barriers can be suggested. To address this concern, this chapter focuses on the interfacial delamination in hybrid multilayer permeation barriers, a critical but largely unexplored issue. Emerging from our computation modeling results is an improved structural design of the multilayer permeation barriers with enhanced mechanical reliability.

4.2 Model

ABAQUS FEA software was used to model barrier layer crack propagation. The models assumed a very thick substrate with material properties equal to the organic layer (PET with an elastic modulus, E_{or}, equal to 2GPa and Poisson's ratio, v_{or}, equal to 0.3). Three layers were bonded to the substrate; the top and bottom layers were fixed-height inorganic layers (AlO_x with an elastic modulus, E_{in}, equal to 300 GPa and Poisson's ratio, v_{in}, equal to 0.3) while the middle layer was an organic layer that varied in height. In some models, an additional layer was added on top called the protective layer as shown in Figure 49. Either 4-node quadrilateral or 3-node tetrahedral plane strain elements were used in the model (depending on the mesh region) since the barrier layer is long in the out-of-plane direction and stretched in the in-plane direction.

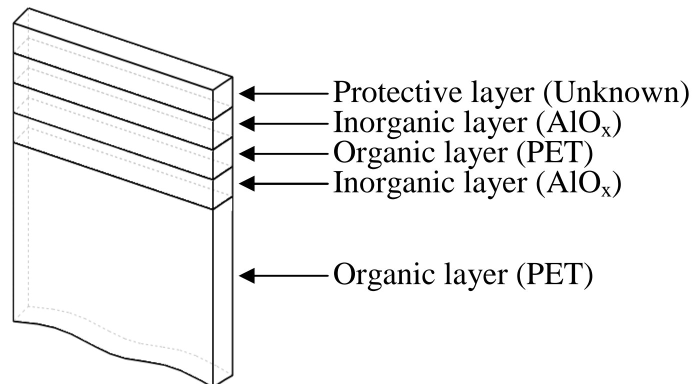

Figure 49. Schematic of hybrid barrier layer model.

The analysis of barrier layer crack propagation in this paper begins exactly where Cordero, Yoon, and Suo left off: a channel crack in the barrier layer [53]. After the brittle crack in the inorganic layer has occurred, the probability of delamination occurring between the inorganic and organic layer is high. Therefore, a model was

created to study the delamination process of the top inorganic layer. Figure 50 shows a schematic of the model used to analyze this delamination. Symmetry was used to model half of the system with the channel crack occurring down the middle. A delamination crack, L, was placed between the inorganic layer and the organic layer. The height ratio, H_r, of the organic layer to the inorganic layer was studied to determine the effects on delamination. The length of the model was 100 times the height of the inorganic layer, *h*, while the delamination crack was varied between 0 and 50 times *h*.

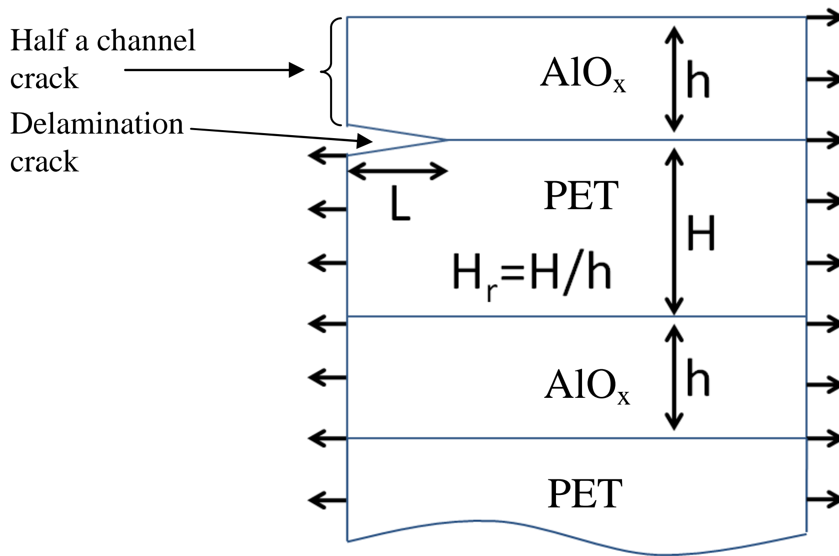

Figure 50. Delamination FEA model setup without a protective layer added to the barrier layer

Next, in an effort to reduce the tendency for delamination crack propagation, a protective layer was added to the model as shown in Figure 51. For this model, H_r was held constant equal to one while the height ratio of the protective layer, H_p, was allowed to vary. The elastic modulus of the inorganic layer and organic layers remained the same as the previous model, but because the protective layer is a new

proposed layer, its elastic modulus was varied between 2MPa and 20GPa with a Poisson's ratio of 0.3.

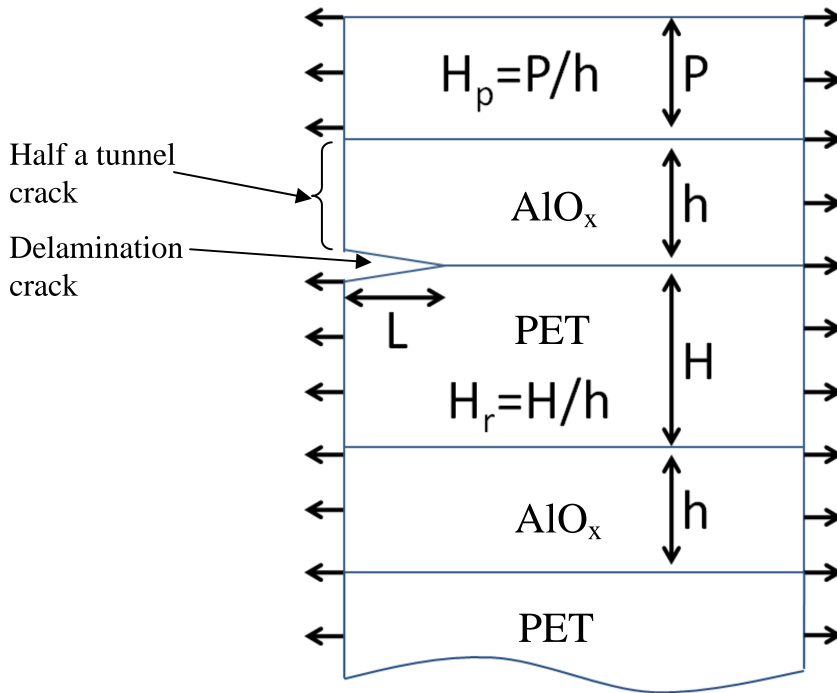

Figure 51. Delamination FEA model setup with protective layer added to the barrier layer

The above figure only incorporated a delamination crack between the inorganic layer and the organic layer. There is a possibility that a delamination crack could form at the interface between the protective layer and the inorganic layer. A third model was created with a delamination crack at both interfaces about the top inorganic layer as shown in Figure 52.

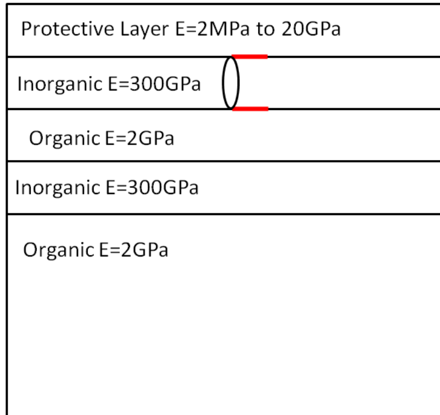

Figure 52. Two delamination cracks in a barrier layer with a protective layer

The focus of the three models previously discussed assumes a channel crack (or tunnel crack as in the last two models) has already occurred in the brittle inorganic layer, therefore, delamination is the next mode of crack propagation. But, since a new layer was added to the barrier layer structure, examination of the channel crack (now a tunnel crack) must be re-evaluated. A fourth set of models were created similar to the models described earlier but without delamination cracks. These models were created to analyze the new driving force for a tunneling crack in the inorganic layer when a protective layer is present and compare that to the driving force of the channel crack without a protective layer.

The method for modeling the crack driving force is depicted in Figure 53. A cross section of the structure well after the crack front has already passed is modeled with the tunnel crack in place. A second model is created showing the layered structure well before the crack front. As the two models are stretched with a tensile displacement perpendicular to the direction of crack propagation, the total resulting strain energies are compared. The difference in total strain energies between the two models shows the driving force for crack propagation.

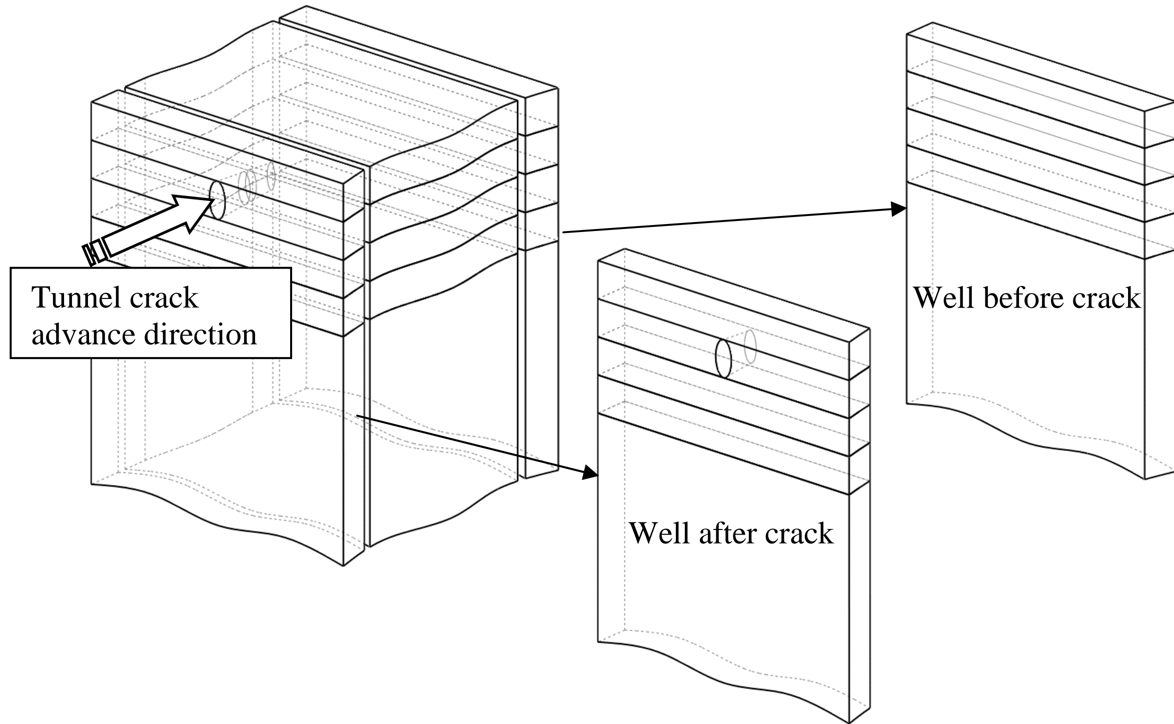

Figure 53. Modeling of a tunneling crack through the inorganic layer of a hybrid barrier layer

4.3 Results

The energy release rate, *G*, was calculated along the normalized delamination crack length, *L/h*. Both the normalized delamination crack length and the normalized height of the organic layer, $H_r = H/h$, were varied to study their dependency on *G* as the structure was prescribed a tensile elongation.

Figure 54 shows the results for a channel crack that has already formed through the top inorganic layer. The normalized energy release rate, $G/(E_{in}\varepsilon^2 h)$, of the delamination crack is plotted versus the delamination length, *L*, normalized by the thickness of the inorganic layer, *h*. The results show that the energy release rate increases steeply as the delamination length becomes small. As the thickness ratio is

increased between the organic and inorganic layer, the energy release rate curve moves to the right and down.

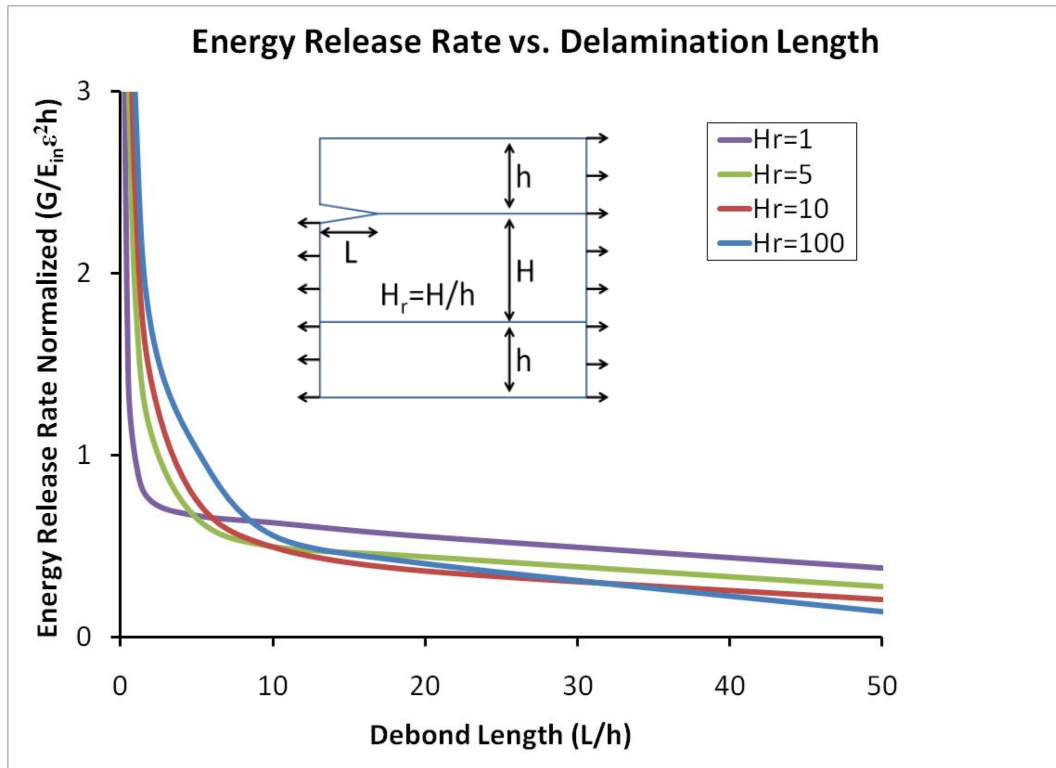

Figure 54. Delamination results for non-protected barrier layers

If the objective is to reduce the tendency for delamination, the thinner organic layer is the optimal choice, which is in agreement with the research conducted by Cordero, Yoon, and Suo [53]. The curve with the thickness ratio, H_r, equal to one creates the shortest delamination length in this configuration as long as the critical normalized energy release rate for this system, $G_c/(E_{in}\varepsilon^2 h)$, is above 0.75. The shorter the delamination length, the less area exposed to possible water vapor transmission.

The FEA model results for the barrier layer with a protective layer on top shows that the protective layer helps decrease the delamination length. Figure 55 depicts the normalized energy release rate of the delamination, $G/(E_{in}\varepsilon^2 h)$, versus the normalized

delamination length for the protective layer, L/h, with various protective layer elastic moduli, E_p. As expected, as the elastic modulus of the protective layer increases, the energy release rate curve shifts lower. As the elastic modulus of the protective layer decreases, the curves move towards the model with no protective layer. This model assumes a well-bonded protective layer as shown in Figure 56.

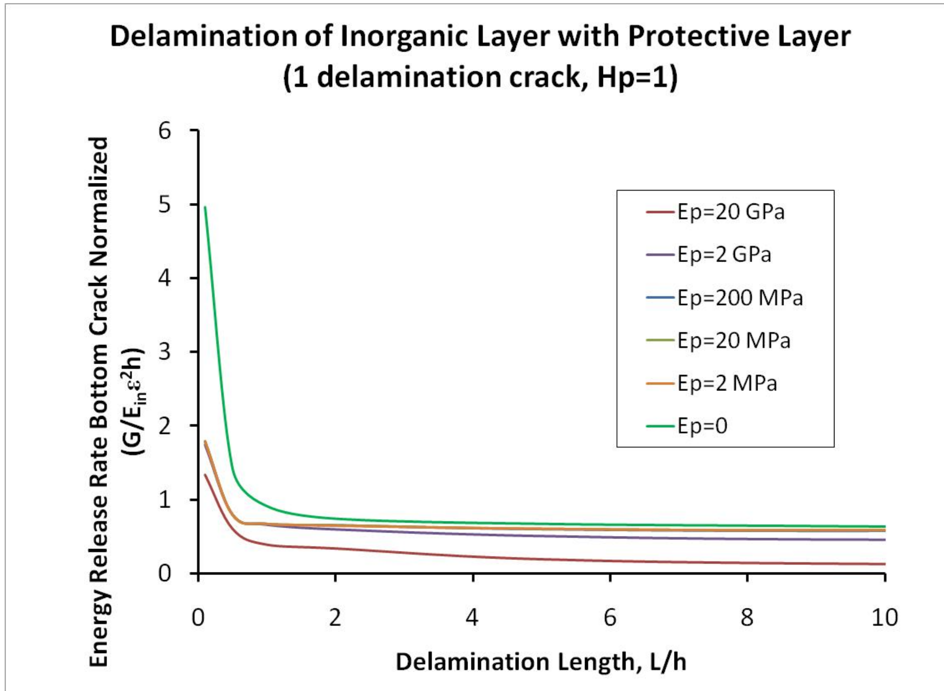

Figure 55. One delamination crack with a protective layer

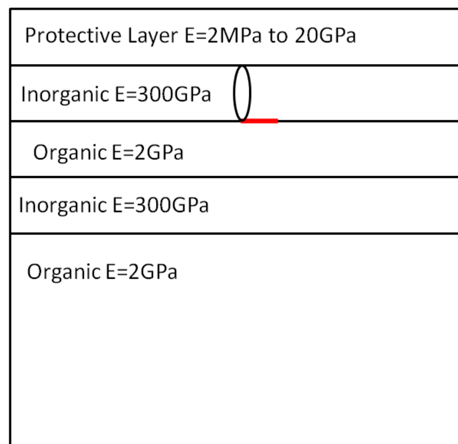

Figure 56. One delamination crack in a barrier layer with a protective layer

Figure 57 below shows three plots, each with a different elastic modulus for the protective layer. As the stiffnesses of the protective layer decrease, the energy release rates increase overall. It is therefore benefitial to apply a protective layer with a higher stiffness. In terms of protective layer thickness, the plots all show that a thicker protection layer is advantageous over a thinner protective layer. It is interesting to note the trend seen in the final plot when E_p = 200MPa. All three thickness ratios tend to follow the same path for a longer delamination length. This reinforces the earlier results that show stiffer, thicker protective layers are preferred when trying to decrease delamination cracks.

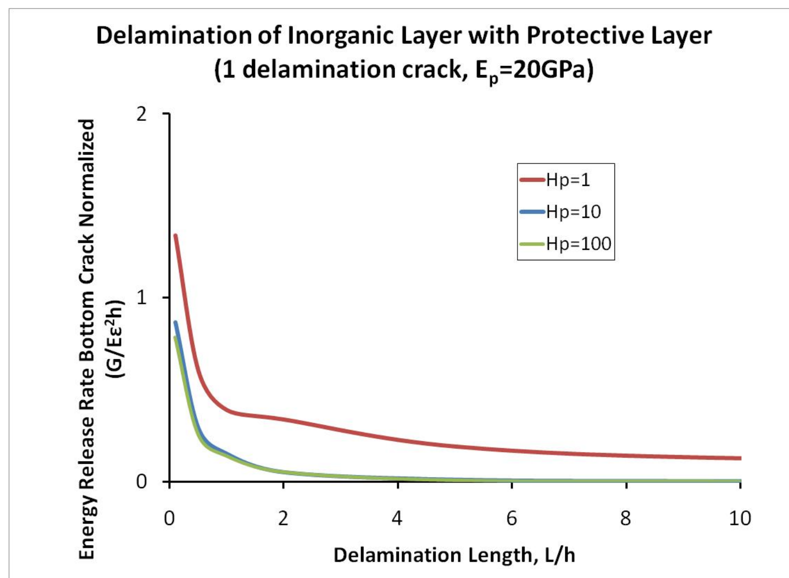

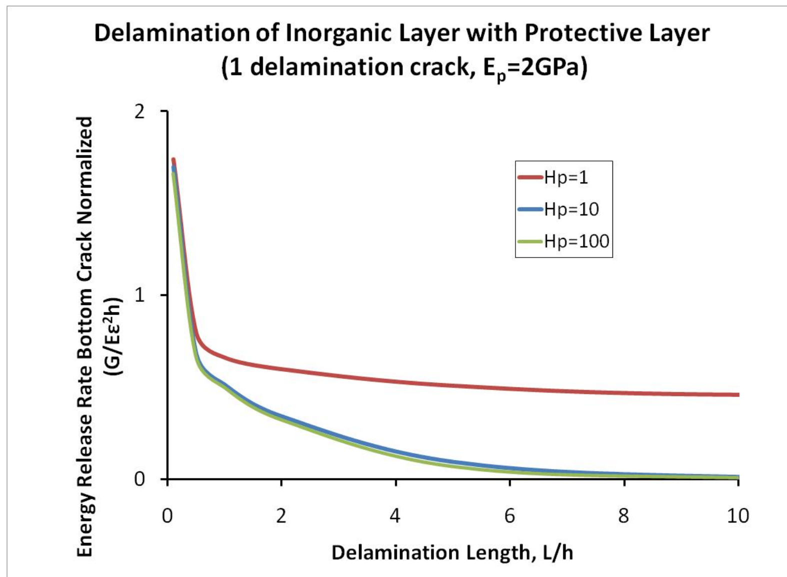

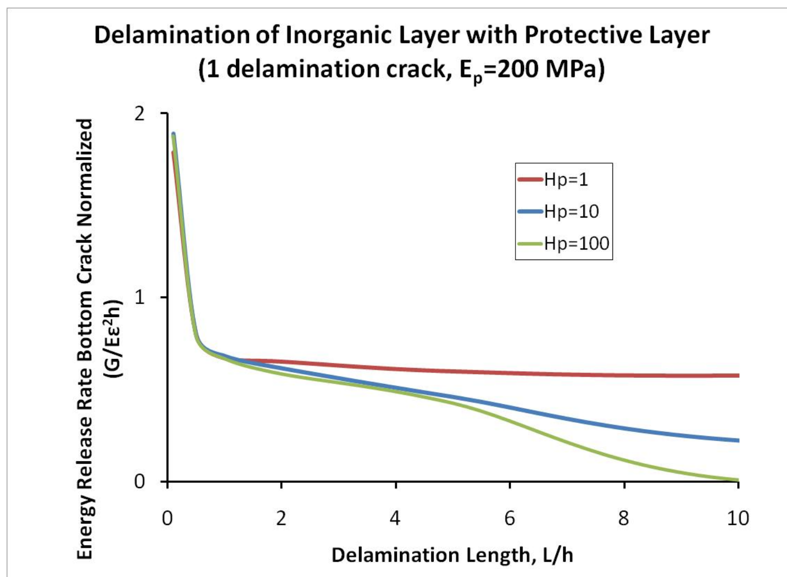

Figure 57. Energy release rate of one delamination crack with various protective layer stiffness

A slightly different model was created to study the effect of two delamination cracks as shown in Figure 52. The results are very similar to the model with only one delamination crack. Figure 58 below shows the results for two delamination cracks and a protective layer thickness ratio equal to one. The only protective layer that reduces the energy release rate of the delamination significantly is the one with a

stiffness of 20 GPa. All other stiffinesses tend to follow the same path which is marginally less than no protective layer (E=0).

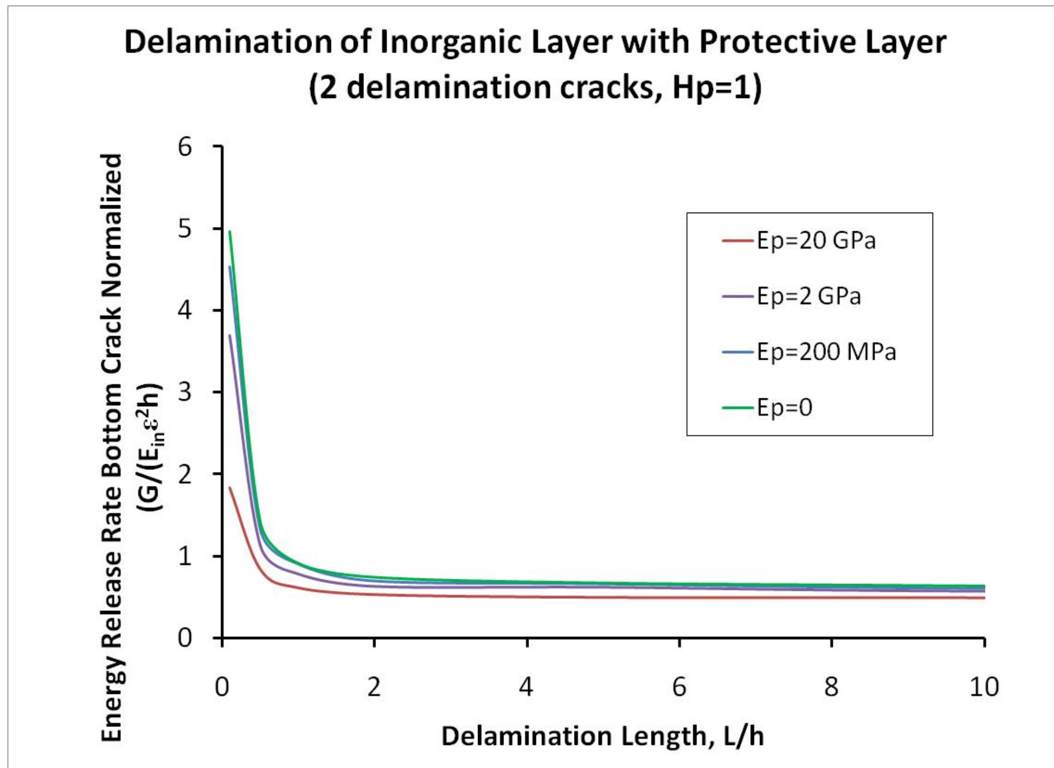

Figure 58. Two delamination cracks with a protective layer

The addition of a protective layer above the top inorganic layer improved the barrier layer structure. The protective layer helped to reduce the normalized energy release rate for the propagation of a delamination crack. The final set of models used to analyze the barrier layer took a step backwards to determine if the protective barrier was instrumental in preventing the channel (or now tunnel) crack in the first place. The normalized energy release rate, $G/(E_{in}\varepsilon^2 h)$, of the tunneling crack for models with various protective layer configurations is shown in Figure 59. The thickness of the protective layer, H_p, had no significant effect on the energy release rate. However, the stiffness of the protective layer, E_p, reduced the energy release rate as the stiffness

increased. The dashed line at the top shows the energy release rate assuming a channel crack formation with no protective layer, portraying the importance of a well-bonded protective layer.

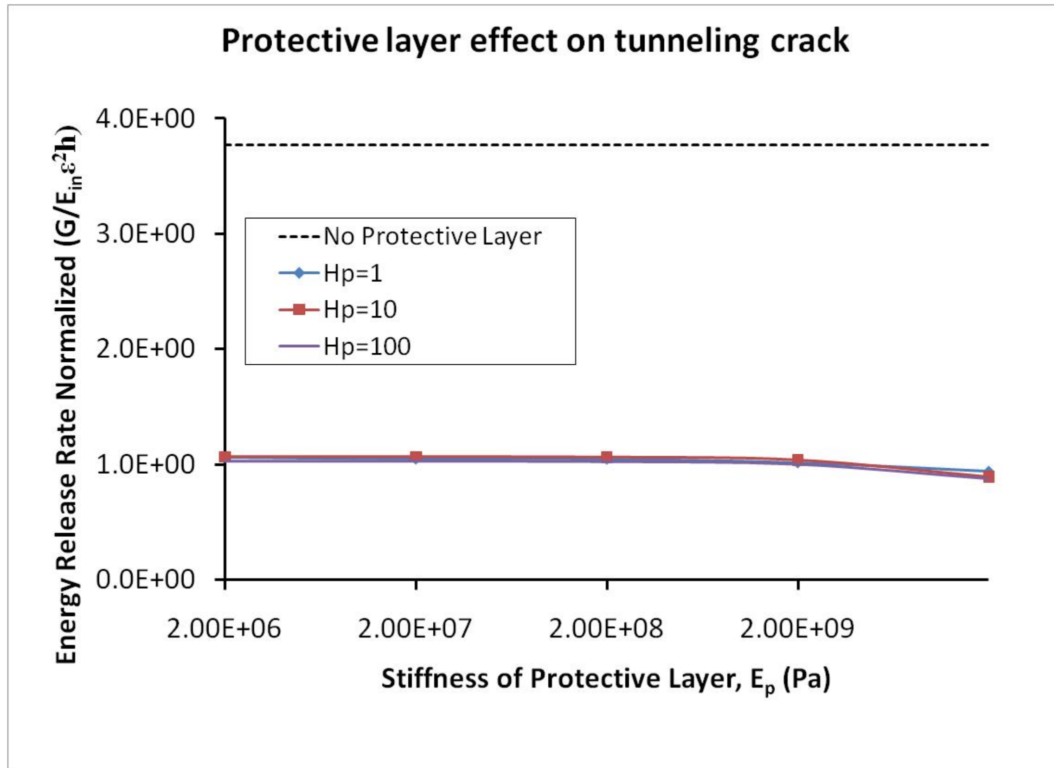

Figure 59. Energy release rate of a tunneling crack through an inorganic layer both with and without a protective layer

4.4 Discussion

It was shown that the energy release rate tended to go to infinity as the delamination length went to zero. This is an abnormal situation since the energy release rate is often bounded. The organic layer in this model is assumed to remain intact, so when the entire model is stretched, the free end of the top inorganic layer where the channel crack is located is free to move while the organic layer just beneath is constrained. Additionally, the organic layer is much more compliant than the inorganic layer.

When the top inorganic layer is pulled with a free end, the entire layer will show general body motion instead of elastic strain. As the delamination length becomes smaller, the length of organic material able to strain to accommodate the general body motion becomes smaller. The same displacement over a smaller length makes the stress rise to infinity.

Adding a protective layer over the top inorganic layer was shown to decrease the potential for two different types of cracks to form. The protective layer significantly reduces the energy release rate of a tunneling crack in the inorganic layer. The reduction of the energy release rate for the tunneling crack was not affected by the thickness of the protective layer or the stiffness of the protective layer. The protective layer mildly reduced the energy release rate of the delamination cracks. The most appealing configuration contains a stiff, thick protective layer although a stiff, thin protective layer also decreased the probability of crack propagation.

4.5 Conclusion

The hybrid barrier layer is an important component for the success of flexible electronic devices. Without the barrier layer, flexible luminescent electronics such as FOLEDs tend to oxidize and fail. The limited research on the failure mechanisms points to water vapor transfer through pin-hole leaks and cracks. Research into delamination cracks suggests that decreasing the length of delamination could reduce the rate of water vapor transmission. FEA modeling shows that thinner organic layers create shorter delamination cracks when barrier layers are stretched. To reduce the tendency for tunneling or delamination cracks, protective layers can be added above inorganic layers in barrier layers. Stiff, thick or thin protective layers reduce the

energy release rate for tunneling crack propagation, while stiff, thick protective layers reduce the energy release rate for delamination crack propagation.

Chapter 5: Concluding Remarks

Flexible electronics are emerging through trade shows, conventions, and limited commercial sales. Tantalizing future aside, flexible electronics still face significant challenges, both mechanical and economical, for their wide spread use. This thesis attempted to contribute to the advancement of flexible electronics field by addressing three different facets of its mechanics challenges.

Summary of research findings:

The major findings of this thesis are summarized as follows:

- Patterned holes in a thin stiff film reduce stress concentration and increase deformability
  - Circular holes densely spaced in a triangular pattern effectively reduce stress concentration.
  - Hidden serpentines among the ligaments deconcentrate the strain normally affecting holes in tension
  - The thin film is initially planar and deflects out-of-plane to accommodate increased tensile deformation
  - A majority of the film deforms elastically thus allows cyclic elongations without fracture
  - The circular hole pattern is easy to manufacture
  - The technology is scalable (does not depend on the length scale), thus can be applied to both circuit and component levels
- Quality printing maps define the defect lengths and interfacial adhesion energy ratios required to create successful transfer printing

    - Introduced defects along the transfer substrate interface can improve successful transfer printing
    - Inherent defects along the device substrate interface can hinder successful transfer printing
    - Interfacial adhesion dominates the quality of transfer printing onto compliant device substrates
    - Interfacial defect size dominates the quality of transfer printing onto stiffer device substrates
- Protective layers reduce barrier layer failure by impeding interfacial crack propagation
    - Interfacial delaminations are highly possible after a channel crack occurs in the inorganic layer of a barrier layer
    - Delamination cracks increase the area exposed to water vapor transfer
    - Protective layers significantly reduce the driving force for delamination cracks
    - Protective layers greatly reduce the driving force for tunneling cracks in the inorganic layers
    - Stiff, thick protective layers are more effective in reducing the driving force for interfacial crack propagation
    - Having a well bonded protective layer is essential to reducing the driving force for interfacial crack propagation

Contributions of this thesis:

Chapter 2 showed the deconcentration of strain in thin stiff films patterned with circular holes by deflecting out-of-plane. Consequently, large elongations induced small strains in the film. Using finite element simulations, we quantified the effects of pattern geometry, loading direction and substrate stiffness on the strain deconcentration in these patterned films. The calculation of the driving force for crack growth near the hole edges further explained the large deformability of the patterned thin stiff films demonstrated in recent experiments. These quantitative results can serve as guidelines in designing flexible thin films patterned with circular holes to satisfy certain deformability criterion.

Furthermore, the general principle of achieving large deformability of thin stiff films by suitably patterning (e.g., circular holes) is essentially geometric, thus independent of materials and length scales. Therefore, such a structural principle can be potentially applied at both device and component levels in designing architecture of flexible electronics. Results show that this easy to manufacture patterning technique addresses the challenges associated with poor deformability of thin films discussed in Chapter 1.

Chapter 3 explored the science underpinning the transfer printing process and thus identified the mechanisms governing transfer printing quality, through comprehensive computational modeling. The outcomes of this study defined a quality map of transfer printing in the space spanned by the critical mechanical properties and geometrical parameters in a transfer printing structure. Some major findings emerging from the quality map are recapped as follows:

(1) While the existing understanding of transfer printing mainly relies on the differential interfacial adhesion [40], the results in this paper suggest that both interfacial defects (e.g., cracks) and differential interfacial adhesion play pivotal roles in transfer printing quality.

(2) Transfer printing onto a stiff device substrate is dominated by the interfacial defects, and is less sensitive to the differential adhesion. In contrast, transfer printing onto a compliant device substrate, although more challenging, can be significantly improved by tailoring the differential interfacial adhesion.

(3) Controlling the interfacial defects offers new pathways to improve transfer printing quality which remain largely unexplored. The results in this paper provide quantitative guidance on interfacial defect control to achieve certain criteria of transfer printing quality.

In summary, the quality map of transfer printing revealed critical mechanical and geometrical parameters that governed the transfer printing process, and offered new insights towards optimal printing conditions. These tools can be used to address the manufacturing challenges associated with flexible electronics discussed in Chapter 1.

Finally, Chapter 4 showed that a stiff, thick protective layer helped decrease the probability of propagating a tunnel crack while reducing the likelihood of material delamination. This provided insight into one of the most elusive challenges faced by flexible electronics – creating a barrier layer that is flexible yet impermeable to water vapor transfer. Since most research into barrier layer failure focused on channel and tunnel cracks, this paper focused on methods for preventing channel cracks and delamination cracks. The reduction of cracks in barrier layers is vital to

the creation of reliable flexible electronic systems. Adding a well-bonded, stiff protective layer to the top of a hybrid barrier layer helped address the reliability issues for luminescent flexible electronics discusses in Chapter 1.

Figure 60 shows the three challenges addressed to help advance the field of flexible electronics. The stretchability of thin films of electronic materials helps create functional layers capable of handling the strains induced by bending, twisting, and stretching electronic devices. The technique to increase transfer printing quality helps reduce the cost of manufacturing as new materials become compatible with transfer printing. Finally, trends towards the reduction of crack propagation in barrier layers provides insight to designers specializing in barrier layer coatings.

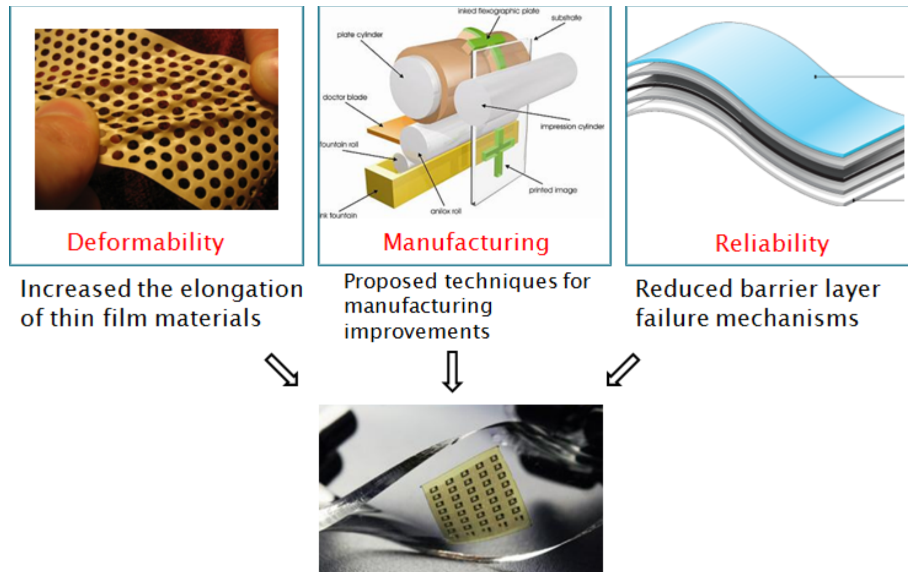

Figure 60. Three enabling technologies addressed to develop flexible electronics; Increased deformability, enhanced manufacturing techniques, and increased reliability through barrier layer coatings.

Publications

Journals:

Tucker, M. B., Li, T. "Strain deconcentration in thin films patterned with circular holes," *International Journal of Applied Mechanics,* 1(4) 1-12, 2009.

Tucker, M. B., Hines, D.R., Li, T. "A quality map of transfer printing," *Journal of Applied Physics*, in press, 2009.

Tucker, M. B., Jia, Z., Li, T. "Failure mechanisms for permeation barriers in flexible electronics", in preparation, 2009.

Conferences:

T. Li, M. Tucker, Stretchable thin films patterned with circular holes: An architecture concept for flexible electronics, Materials Research Society Fall Meeting, San Francisco, CA, March 2008.

T. Li, M. Tucker, Stretchable thin films patterned with circular holes, ASME International Mechanical Engineering Congress, Boston, MA, November 2008.

T. Li, M. Tucker, Effect of interfacial defects on transfer printing process for fabrication of flexible electronics, Accepted, ASME International Mechanical Engineering Congress, Lake Buena Vista, FL, November 2009.

Bibliography

[1] G. Dennler and N. Sariciftci, “Flexible Conjugated Polymer-Based Plastic Solar Cells: From Basics to Applications,” *Proceedings of the IEEE*, vol. 93, 2005, pp. 1429-1439.

[2] S.R. Forrest, “The path to ubiquitous and low-cost organic electronic appliances on plastic,” *Nature*, vol. 428, Apr. 2004, pp. 911-918.

[3] J.A. Rogers and Z. Bao, “Printed plastic electronics and paperlike displays,” *Journal of Polymer Science Part A: Polymer Chemistry*, vol. 40, 2002, pp. 3327-3334.

[4] T. Someya, T. Sekitani, S. Iba, Y. Kato, H. Kawaguchi, and T. Sakurai, “A large-area, flexible pressure sensor matrix with organic field-effect transistors for artificial skin applications,” *Proceedings of the National Academy of Sciences of the United States of America*, vol. 101, Jul. 2004, pp. 9966-9970.

[5] S. Wagner, S.P. Lacour, J. Jones, P.I. Hsu, J.C. Sturm, T. Li, and Z. Suo, “Electronic skin: architecture and components,” *Physica E: Low-dimensional Systems and Nanostructures*, vol. 25, Nov. 2004, pp. 326-334.

[6] G.H. Gelinck, H.E.A. Huitema, E. van Veenendaal, E. Cantatore, L. Schrijnemakers, J.B.P.H. van der Putten, T.C.T. Geuns, M. Beenhakkers, J.B. Giesbers, B. Huisman, E.J. Meijer, E.M. Benito, F.J. Touwslager, A.W. Marsman, B.J.E. van Rens, and D.M. de Leeuw, “Flexible active-matrix displays and shift registers based on solution-processed organic transistors,” *Nat Mater*, vol. 3, Feb. 2004, pp. 106-110.

[7] S. Suresh, *Fatigue of materials*, Cambridge University Press, 1998.

[8] T. Ando, M. Shikida, and K. Sato, “Tensile-mode fatigue testing of silicon films as structural materials for MEMS,” *Sensors and Actuators A: Physical*, vol. 93, Aug. 2001, pp. 70-75.

[9] M.A. Haque, M.T.A. Saif, and J.D. Achenbach, “Deformation Mechanisms in Free-Standing Nanoscale Thin Films: A Quantitative in situ Transmission Electron Microscope Study,” *Proceedings of the National Academy of Sciences of the United States of America*, vol. 101, Apr. 2004, pp. 6335-6340.

[10] P.C. Bouten, P.J. Slikkerveer, and Y. Leterrier, “Mechanics of ITO on plastic substrates for flexible electronics,” *Flexible Flat Panel Displays*, G.P. Crawford, ed., John Wiley and Sons, 2005, pp. 99-120.

[11] T. King and K. Saraswat, “Low-temperature (< 550°C) fabrication of poly-Si thin-film transistors,” *Electron Device Letters, IEEE*, vol. 13, 1992, pp. 309-311.

[12] O. Nuyken, S. Jungermann, V. Wiederhirn, E. Bacher, and K. Meerholz, "Modern Trends in Organic Light-Emitting Devices (OLEDs)," *Monatshefte für Chemie / Chemical Monthly*, vol. 137, Jul. 2006, pp. 811-824.

[13] D. Kolosov, D.S. English, V. Bulovic, P.F. Barbara, S.R. Forrest, and M.E. Thompson, "Direct observation of structural changes in organic light emitting devices during degradation," *Journal of Applied Physics*, vol. 90, Oct. 2001, pp. 3242-3247.

[14] P.E. Burrows, V. Bulovic, S.R. Forrest, L.S. Sapochak, D.M. McCarty, and M.E. Thompson, "Reliability and degradation of organic light emitting devices," *Applied Physics Letters*, vol. 65, Dec. 1994, pp. 2922-2924.

[15] B.D. Vogt, H. Lee, V.M. Prabhu, D.M. DeLongchamp, E.K. Lin, W. Wu, and S.K. Satija, "X-ray and neutron reflectivity measurements of moisture transport through model multilayered barrier films for flexible displays," *Journal of Applied Physics*, vol. 97, Jun. 2005, pp. 114509-7.

[16] P.I. Hsu, M. Huang, Z. Xi, S. Wagner, Z. Suo, and J.C. Sturm, "Spherical deformation of compliant substrates with semiconductor device islands," *Journal of Applied Physics*, vol. 95, Jan. 2004, pp. 705-712.

[17] R. Bhattacharya, S. Wagner, Yeh-Jiun Tung, J. Esler, and M. Hack, "OLED pixel array on a dome," *Electron Devices Meeting, 2004. IEDM Technical Digest. IEEE International*, 2004, pp. 385-388.

[18] S.P. Lacour, S. Wagner, R.J. Narayan, T. Li, and Z. Suo, "Stiff subcircuit islands of diamondlike carbon for stretchable electronics," *Journal of Applied Physics*, vol. 100, Jul. 2006, pp. 014913-6.

[19] T. Li, Z. Huang, Z. Suo, S. Lacour, and S. Wagner, "Stretchability of thin metal films on elastomer substrates," *Applied Physics Letters*, vol. 85, 2004, pp. 3437, 3435.

[20] S.P. Lacour, S. Wagner, Z. Huang, and Z. Suo, "Stretchable gold conductors on elastomeric substrates," *Applied Physics Letters*, vol. 82, Apr. 2003, pp. 2404-2406.

[21] W.M. Choi, J. Song, D. Khang, H. Jiang, Y.Y. Huang, and J.A. Rogers, "Biaxially Stretchable "Wavy" Silicon Nanomembranes," *Nano Letters*, vol. 7, Jun. 2007, pp. 1655-1663.

[22] D. Khang, H. Jiang, Y. Huang, and J.A. Rogers, "A Stretchable Form of Single-Crystal Silicon for High-Performance Electronics on Rubber Substrates," *Science*, vol. 311, Jan. 2006, pp. 208-212.

[23] S. Lacour, J. Jones, S. Wagner, T. Li, and Z. Suo, "Stretchable Interconnects for Elastic Electronic Surfaces," *Proceedings of the IEEE*, vol. 93, 2005, pp. 1459-1467.

[24] Y. Sun and J.A. Rogers, "Inorganic Semiconductors for Flexible Electronics," *Advanced Materials*, vol. 19, 2007, pp. 1897-1916.

[25] T. Li, Z. Suo, S. Lacour, and S. Wagner, "Compliant thin film patterns of stiff materials as platforms for stretchable electronics," *Journal of Materials Research*, vol. 20, Dec. 2005, pp. 3277, 3274.

[26] S.P. Lacour, D. Chan, S. Wagner, T. Li, and Z. Suo, "Mechanisms of reversible stretchability of thin metal films on elastomeric substrates," *Applied Physics Letters*, vol. 88, May. 2006, pp. 204103-3.

[27] P. Mandlik, S. Lacour, J. Li, S. Chou, and S. Wagner, "Fully elastic interconnects on nanopatterned elastomeric substrates," *Electron Device Letters, IEEE*, vol. 27, 2006, pp. 650-652.

[28] S. Wagner and J. Jones, "Unpublished," 2008.

[29] T. Li, Z. Huang, Z. Xi, S. Lacour, S. Wagner, and Z. Suo, "Delocalizing strain in a thin metal film on a polymer substrate," *Mechanics of Materials*, vol. 37, 2005, pp. 273, 261.

[30] K.J. Hsia, Y. Huang, E. Menard, J. Park, W. Zhou, J. Rogers, and J.M. Fulton, "Collapse of stamps for soft lithography due to interfacial adhesion," *Applied Physics Letters*, vol. 86, Apr. 2005, pp. 154106-3.

[31] Y.Y. Huang, W. Zhou, K.J. Hsia, E. Menard, J. Park, J.A. Rogers, and A.G. Alleyne, "Stamp Collapse in Soft Lithography," *Langmuir*, vol. 21, 2005, pp. 8058-8068.

[32] H. Sirringhaus, T. Kawase, R.H. Friend, T. Shimoda, M. Inbasekaran, W. Wu, and E.P. Woo, "High-Resolution Inkjet Printing of All-Polymer Transistor Circuits," *Science*, vol. 290, Dec. 2000, pp. 2123-2126.

[33] P. Calvert, "Inkjet Printing for Materials and Devices," *Chemistry of Materials*, vol. 13, Oct. 2001, pp. 3299-3305.

[34] T. Kawase, H. Sirringhaus, R.H. Friend, and T. Shimoda, "Inkjet Printed Via-Hole Interconnections and Resistors for All-Polymer Transistor Circuits," *Advanced Materials*, vol. 13, 2001, pp. 1601-1605.

[35] T. Kawase, T. Shimoda, C. Newsome, H. Sirringhaus, and R.H. Friend, "Inkjet printing of polymer thin film transistors," *Thin Solid Films*, vol. 438-439, Aug. 2003, pp. 279-287.

[36] M. Chabinyc, W. Wong, A. Arias, S. Ready, R. Lujan, J. Daniel, B. Krusor, R. Apte, A. Salleo, and R. Street, “Printing Methods and Materials for Large-Area Electronic Devices,” *Proceedings of the IEEE*, vol. 93, 2005, pp. 1491-1499.

[37] J. Wilbur, A. Kumar, E. Kim, and G. Whitesides, “Microfabrication by microcontact printing of self-assembled monolayers,” *Advanced Materials*, vol. 6, 1994, pp. 600-604.

[38] Y. Xia, J.A. Rogers, K.E. Paul, and G.M. Whitesides, “Unconventional Methods for Fabricating and Patterning Nanostructures,” *Chemical Reviews*, vol. 99, Jul. 1999, pp. 1823-1848.

[39] A. Kumar and G.M. Whitesides, “Features of gold having micrometer to centimeter dimensions can be formed through a combination of stamping with an elastomeric stamp and an alkanethiol ``ink'' followed by chemical etching,” *Applied Physics Letters*, vol. 63, Oct. 1993, pp. 2002-2004.

[40] D.R. Hines, V.W. Ballarotto, E.D. Williams, Y. Shao, and S.A. Solin, “Transfer printing methods for the fabrication of flexible organic electronics,” *Journal of Applied Physics*, vol. 101, Jan. 2007, pp. 024503-9.

[41] X. Feng, M.A. Meitl, A.M. Bowen, Y. Huang, R.G. Nuzzo, and J.A. Rogers, “Competing fracture in kinetically controlled transfer printing,” *Langmuir: The ACS Journal of Surfaces and Colloids*, vol. 23, Dec. 2007, pp. 12555-60.

[42] S.L. Chiu, J. Leu, and P.S. Ho, “Fracture of metal-polymer line structures. I. Semiflexible polyimide,” *Journal of Applied Physics*, vol. 76, Nov. 1994, pp. 5136-5142.

[43] H.-. Yu, M.Y. He, and J.W. Hutchinson, “Edge effects in thin film delamination,” *Acta Materialia*, vol. 49, Jan. 2001, pp. 93-107.

[44] B. Erdem Alaca, M.T.A. Saif, and H. Sehitoglu, “On the interface debond at the edge of a thin film on a thick substrate,” *Acta Materialia*, vol. 50, Mar. 2002, pp. 1197-1209.

[45] N. Lu, J. Yoon, and Z. Suo, “Delamination of stiff islands patterned on stretchable substrates,” *International Journal of Material Research*, vol. 98, 2007, pp. 717-722.

[46] T. Li and Z. Suo, “Deformability of thin metal films on elastomer substrates,” *International Journal of Solids and Structures*, vol. 43, Apr. 2006, pp. 2351-2363.

[47] H. Mei, R. Huang, J.Y. Chung, C.M. Stafford, and H. Yu, “Buckling modes of elastic thin films on elastic substrates,” *Applied Physics Letters*, vol. 90, Apr. 2007, pp. 151902-3.

[48] J. Lewis and M. Weaver, "Thin-film permeation-barrier technology for flexible organic light-emitting devices," *Selected Topics in Quantum Electronics, IEEE Journal of*, vol. 10, 2004, pp. 45-57.

[49] C. Lungenschmied, G. Dennler, H. Neugebauer, S.N. Sariciftci, M. Glatthaar, T. Meyer, and A. Meyer, "Flexible, long-lived, large-area, organic solar cells," *Solar Energy Materials and Solar Cells*, vol. 91, Mar. 2007, pp. 379-384.

[50] L. Zambov, K. Weidner, V. Shamamian, R. Camilletti, U. Pernisz, M. Loboda, G. Cerny, D. Gidley, H. Peng, and R. Vallery, "Advanced chemical vapor deposition silicon carbide barrier technology for ultralow permeability applications," *Journal of Vacuum Science & Technology A: Vacuum, Surfaces, and Films*, vol. 24, 2006, pp. 1706-1713.

[51] A.B. Chwang, M.A. Rothman, S.Y. Mao, R.H. Hewitt, M.S. Weaver, J.A. Silvernail, K. Rajan, M. Hack, J.J. Brown, X. Chu, L. Moro, T. Krajewski, and N. Rutherford, "Thin film encapsulated flexible organic electroluminescent displays.," *Applied Physics Letters*, vol. 83, Jul. 2003, p. 413.

[52] G.L. Graff, P.E. Burrows, R.E. Williford, and R.F. Praino, "Barrier Layer Technology for Flexible Displays," *Flexible Flat Panel Displays*, G.P. Crawford, ed., John Wiley and Sons, 2005, pp. 57-77.

[53] Cordero, Nicolals, Yoon, Juil, and Suo, Zhigang, "Channel cracks in a hermetic coating consisting of organic and inorganic layers," *Applied Physics Letters*, vol. 90, Mar. 2007, pp. 1-3.